Charles University in Prague

Faculty of Science

MASTER THESIS

Bc. Miroslav Soroka

Structure and thermoelectric properties of layered cobaltate

Strukturní a termoelektrické vlastnosti vrstevnatých kobaltátů

Department of Inorganic Chemistry

Supervisor: RNDr. Daniel Nižňanský, Dr.

Consultants: Ing. Josef Buršík CSc., RNDr. Karel Knížek Dr.

Study programme: Inorganic Chemistry

Prague, 2016

Tato diplomová práce byla podpořena Grantovou Agenturou České Republiky pod projektem č. 13-03708 S a 14-18392 S.

This work was supported by the Grant Agency of Academy of science of the Czech Republic under Grant no. 13-03708 S and 14-18392 S.

Prohlášení:

Prohlašuji, že jsem tuto diplomovou práci vypracoval samostatně a že jsem uvedl všechny použité informační zdroje a literaturu. Táto práce ani její podstatná část nebyla předložená k získání jiného nebo stejného akademického titulu

I declare that I carried out this diploma thesis independently and I cited all used information sources and literature. Neither this work nor its essential part was proposed with aim to obtain another or the same academic degree.

In Prague, 25. 8. 2016 Miroslav Soroka

Název práce: Strukturní a termoelektrické vlastnosti vrstevnatých kobaltátů

Autor: Miroslav Soroka

Katedra: Katedra anorganické chemie, PřF UK, Praha

Vedoucí diplomové práce: RNDr. Daniel Nižňanský, Dr.

Konzultant: Ing. Josef Buršík, CSc., RNDr. Karel Knížek Dr.

e-mail vedoucího: niznansk@natur.cuni.cz

Abstrakt

Předložená práce se zabývá přípravou Na_xCoO_2 výchozím obsahem sodíku x = 1.0, 0.9, 0.8 a 0.7 pomocí Pechiniho metody. Vzorky byly žíhané v teplotním rozsahu od 550 °C do 750 °C. Připravené vzorky byly strukturně charakterizovány pomoci práškové rentgenové difrakce (PXRD). Prvkové složení bylo určeno pomocí atomové absorpční spektroskopie. Seebeckův koeficient a Weissova konstanta byly určeny pro sérii vzorků obsahujících α- a γ- fázi Na_xCoO_2. PXRD analýza a měření Seebeckova koeficientu ukázalo, že skutečný obsah sodíku ve vrstevnatém kobaltátu je nezávislý na výchozí stechiometrii reakční směsi a reálná stechiometrie sodíku v Na_xCoO_2 se pohybovala v rozmezí od x= 0.65 do 0.75. Z měření magnetizace byla zjištěna přítomnost spinelové fáze ve vzorcích α- fáze, která také vykazovala nezvykle vysoké hodnoty Weissovy konstanty v porovnání se strukturně podobnou γ- fázi Na_xCoO_2.

Byly rovněž připraveny tenké vrstvy Na_xCoO_2 s výchozím obsahem sodíku x = 1.0, 0.52, 0.32 a 0.175 na 00l-orientované podložce α-Al_2O_3 pomocí CSD metody s využitím spin-coating depozice. Byl studován vznik 00l-orientované vrstvy Na_xCoO_2 a také nová metoda pro přípravu *hhh*-orientovaných Co_3O_4 tenkých vrstev. Orientace připravených vrstev byla charakterizována pomocí Ω- křivek a orientace Co_3O_4 v rovině substrátu byla studována pomocí měření φ- skenů. K studiu mikrostruktury a morfologie připravených vrstev byla využita skenovací elektronová mikroskopie a mikroskopie atomárních sil.

Title:	Structure and thermoelectric properties of layered cobaltates
Author:	Miroslav Soroka
Department:	Department of Inorganic Chemistry, Faculty of Science, Charles University of Prague
Supervisor:	RNDr. Daniel Nižňanský, Dr.
Consultant:	Ing. Josef Buršík, CSc., RNDr. Karel Knížek Dr.
Supervisor´s e-mail address:	niznansk@natur.cuni.cz

Abstract

The synthesis of Na_xCoO_2 by Pechini method (with initial sodium stoichiometry x = 1.0, 0.9, 0.8, and 0.7) was studied for the samples heat-treated in the temperature range from 550 °C to 750 °C. The structure characterization and phase composition was carried out by the powder X-ray diffraction (XRD) analysis. The elementary analysis was done using atomic absorption spectroscopy. From the thermoelectric properties, the Seebeck coefficient was measured for both α- and γ- phase. The Weiss constant was determined for α- and γ- phase by linear regression of $1/\chi$. The real sodium content in sodium cobaltate phase was found to be independent on initial sodium precursor weight and measurement by PXRD and Seebeck coefficient showed that the sodium content in Na_xCoO_2 falls in the range from x = 0.65 to 0.75. The magnetization measurements showed presence of spinel Co_3O_4 impurities in the samples and the analysis of magnetic susceptibility showed unusual high values of the Weiss constant for α- phase in comparison with structurally similar γ- Na_xCoO_2.

Thin film of Na_xCoO_2 with initial sodium stoichiometry x = 1.0, 0.52, 0.32, and 0.175 was deposited by chemical solution deposition method using spin-coating deposition on a 00l-oriented α-Al_2O_3 single crystal substrate. The formation and structure characterization of 00l-oriented Na_xCoO_2 and the novel procedure for preparation of *hhh*-oriented Co_3O_4 films by decomposition of 00l-oriented Na_xCoO_2 is reported. The degree of preferred orientation in both materials was determined by XRD Ω- scans and the in- plane orientation of Co_3O_4 was characterized by XRD φ- scans and pole figure measurements. The microstructure morphology of the both materials were investigated using scanning electron microscopy and atomic force microscopy.

Keywords: cobaltates, thermoelectric properties, X-ray diffraction

Klíčová slova: kobaltáty, termoelektrické vlastnosti, rtg. diftrakce

Content

1. Introduction

Effort to reduce our dependence on fossil fuels and reduce greenhouse gas emissions is one of important challenges for science and leads to the development of alternative energy technologies. One of the possible ways to reducing greenhouse emission is better fuel management and higher energy efficiency. Thermoelectricity presents the way to reach it by direct conversion of waste heat to electricity [1]-[3]. This renewed interest in thermoelectric materials is mainly connected with potential application in car industry due to recovery of energy of the waste heat from gasoline and diesel engines [4]. In addition, thermoelectric materials can be also used for direct thermoelectric cooling or heating without necessity of moving parts or fluids [5] [6].

The research at the field of thermoelectricity start at the beginning of 19th century when Thomas J. Seebeck observed voltage difference when two different materials are connected together and the junctions are held at different temperature [7]. The voltage difference is proportional to temperature difference. The ratio of incurred voltage to temperature gradient $\Delta V/T\Delta$ is called Seebeck coefficient α and it is issue of materials. Seebeck coefficient of metals is very low (only a few μV/K). On the other hand, semiconductors have much higher Seebeck coefficient (typically few hundred μV/K). Semiconductors can exhibit either electron conduction (negative thermopower) or hole conduction (positive thermopower). The revers Peltier effect was discovered few years later. The both effects are related to each other by definition:

$$\Pi = \alpha \cdot \mathrm{T}$$

where Π is the Peltier coefficient. The efficiency of TE devices is characterized by figure of merit:

$$zT = \sigma S^2 T/(\kappa_l + \kappa_e)$$

where σ is the electric conductivity, S is the Seebeck coefficient, T stands for operating temperature and κ_l and κ_e are the lattice and electronic thermal conductivity. The above equation clearly shows that the prerequisite for effective thermoelectric materials is a low thermal conductivity. The challenge on field of thermoelectric materials research is to limit the conduction of heat by phonons, without simultaneously reducing the charge transport [8]. Moreover, for good TE material, not only high ZT over a wide temperature range is required, but also sound mechanical, metallurgical and thermal characteristic to be used in practical TE devices.

From an electronic point of view, these materials can be classified as metals, semiconductors and insulator, as materials with zero, small and large band gaps. If we compare the TE properties of these materials, we see that insulators have very high Seebeck coefficient, but extremely low electric conductivity prevents the minimization of σS^2. On the other hand, metals

have high electric conductivity, but their high thermal conductivity and low Seebeck coefficient do not make them the most desirable material for TE applications. The ideal TE material combines relatively high Seebeck coefficient of semiconductors with high electric conductivity of metals [8] (See Figure 1).

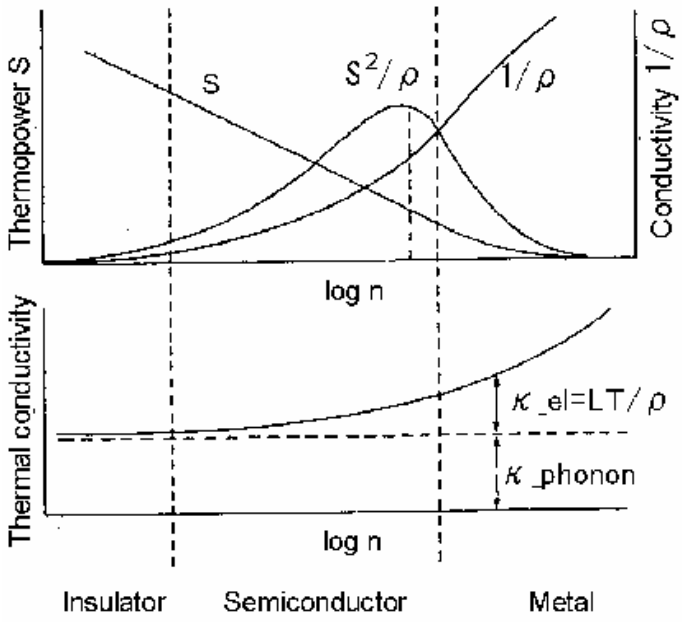

Figure 1. Thermoelectric parameters as a function of temperature [9].

The development of TE materials begins exactly from simple metal semiconductors such as group III-V and group V [10]. The first peak of increased interest in thermoelectric materials can be observed around 1960, that was associated with the discovery of thermoelectric properties of nowadays conventional materials such as Bi_2Te_3 and PbTe. Renewed interest starting in 1990 is connected with synthesis of several types of complex structure materials as skutterudites [11], clathrates [12], half-Heustler alloys [13], complex chalcogenides [14], cobaltates [9], [15][17] and low dimensional thermoelectrics (quantum well and dot, nanowires and molecular junctions) [18].

Until the discovery of Na_xCoO_2 as a good thermoelectric material in 1997, [9] [19] [20] oxide materials did not attract great attentions in TE application, because of their limited thermoelectric performance. The change came when a high Seebeck coefficient was demonstrated in combination with a low resistivity [19] [20] in the case of $NaCo_2O_4$. These works led to increased interest of oxides as thermoelectric materials, which is supported by the promising advantages of oxide materials for thermoelectric applications. Many of the oxides are non-toxic and they have a

good chemical and thermal stability, in contrast to the telluride-based materials. This makes them very suitable for high temperature thermoelectric applications. Additionally, many oxides contain only relatively abundant elements and they are suitable for large scale fabrication and applications. After those first reports of Na_xCoO_2, related compounds, such as $Ca_3Co_4O_9$, were also identified as good thermoelectric materials [21] [22]. These cobaltate materials show a similar high Seebeck coefficient together with a good electrical conductivity. Even though the layered cobaltates are promising oxide thermoelectric materials, they represent only p-type materials., Also other oxides have been studied, because of the necessity of both p- and n-type thermoelectric materials for applications. The main candidates as n-type thermoelectric oxides are ZnO and $SrTiO_3$ [2]. The electronic properties of Al-doped ZnO are very promising and thermoelectric power factors of 20 $\mu W/K^2cm$, comparable to conventional thermoelectric materials can be obtained, however the challenge is to reduce its high thermal conductivity of 40 W/mK [23]. By doping of Al and Ga to $Zn_{0.96}Al_{0.02}Ga_{0.02}O$, a maximum ZT value of 0.6 was achieved at 1273 K [24].

2. Literature review

This chapter provides review about structure and synthesis methods used for preparation of layered cobaltate Na_xCoO_2. Significant attention is dedicated to studies of physical properties especially thermoelectric and magnetic. A brief review about works is done in the field of thin films.

2.1. Structure of Na_xCoO_2

Na_xCoO_2 belongs to a bronze-type compound expressed as A_xBO_2. The structure of Na_xCoO_2 consist of edge-shared octahedrons layers of CoO_2 separated by intercalated sodium ions. As *Fouassier et al*. showed in his work about metal bronzes from 1973, that there are four slightly different layered sodium cobaltate phases depending on sodium stoichiometry: α (*O*3), α´(*O´*3 or *O*1), β (*P´*3 or *P*1) and thermodynamically stable *γ*-phase (*P*2) [25]. [1]

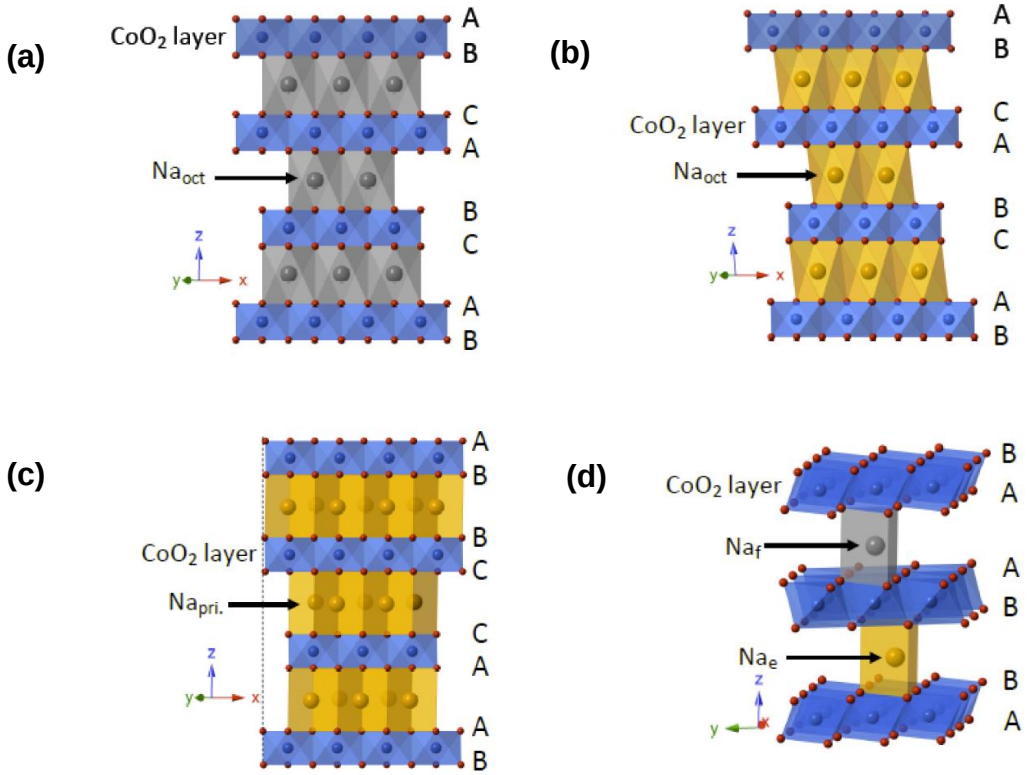

Figure 2. Four structures of layered cobaltates, with depicted oxygen stacking and sodium coordination: a) *α*-phase, b) *α´*-phase, c) *β*-phase, d) *γ*- phase.

[1] The notation in brackets was firstly introduced by *Delmas et al.* whereby first letter (*P*, *T*, *O*) refers to the nature of site occupied by alkali metal ion (prismatic, tetrahedral and octahedral) and the number indicate number of alkali layers in repeated unit (unit cell), apostrophe marks distortions[26].

The oxygen, cobalt and sodium stacking depends on crystalline phase. Table 1 summarized structural information of layered phases. The dependence of lattice parameter on sodium stoichiometry (Fig. 3) was investigated by *Krockenberger et al*. He showed that with increasing sodium content in the structure, the lattice parameter in direction *c* decreases linearly. With increasing sodium contents, positive charge is concentrated between the CoO_2 layers, and as a result, the *c* axis shrinks. The a-axis parameter increases with increasing sodium content, but it varies only about 20 pm throughout the whole sodium stoichiometry [27]. *Berthelot et al*. also showed by in-situ X-ray diffraction, that lattice parameter of *γ*- phase in direction c depends on sodium stoichiometry (Figure 3), but as we can see from the plot, the dependency is not linear but the lattice parameter decrease stepwise with increasing sodium content [28].

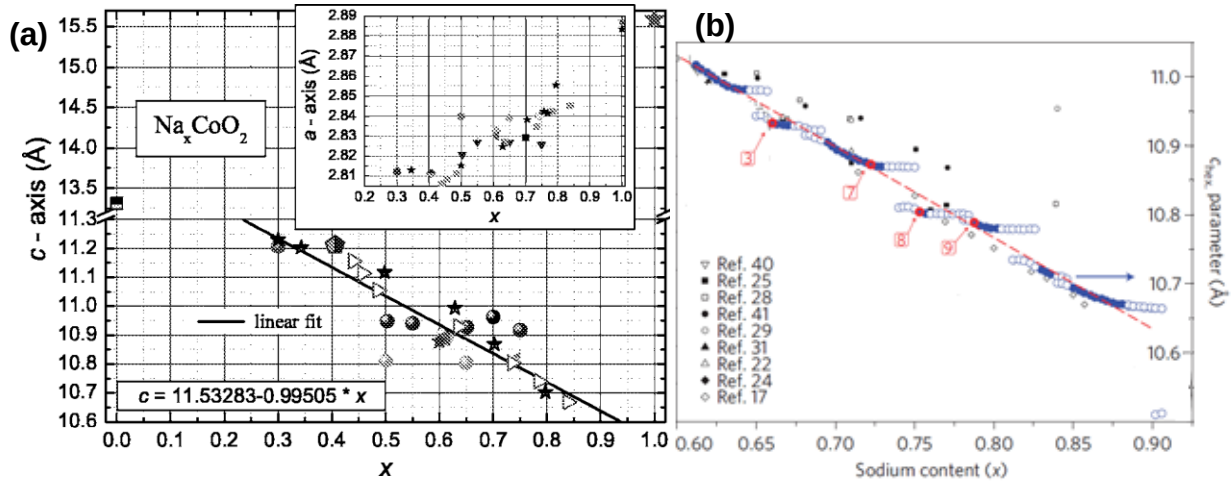

Figure 3. (a) The linear dependence of lattice parameter in direction c and a on sodium stoichiometry published by *Krockenberger et al*. [27], (b) The lattice parameter c dependence on sodium content presented by *Berthelot et al.* [28].

Table 1. Summary of structure information of Na_xCoO_2 phases.

phase	Crystal system	Space group	Oxygen stacking	Sodium coordination	Number of layers	Sodium stoichiometry x
α (*O*3)	rhombohedral	*R-3m*	A-B-C	octahedral	3	$0.9 \leq x \geq 1.0$
α′(*O*′3)	monoclinic	*C2/m*	A-B-C	octahedral	3	$x = 0.75$
β (*P*′3 or *P*1)	monoclinic	*C2/m*	A-B-B-C	prismatic	3	$0.55 \leq x \geq 0.6$
γ (*P2*)	hexagonal	*P6₃/mmc*	A-B-B-A	prismatic	2	$x \sim 0.7$

2.2.Physical properties of Na_xCoO_2

Sodium cobaltate has become the subject of physical studies since its discovery. The sodium dependence of physical properties of Na_xCoO_2 has been investigated by several groups. It is well known, that Na_xCoO_2 with full sodium content ($x = 1$) is a band insulator with Co^{3+} ions in the low spin state t^6_{2g}, whereas sodium deficient systems with cobalt ions in the mixed low spin Co^{3+}/Co^{4+} valence show a wide variety of behavior. A distinct property of the Co ions in the large crystal field induced by their oxygen octahedral environment in the CoO_2 structure, is that the t_{2g} triplet of the Co site is much lower in energy than the e_g doublet, so that the electronic structure of the Co ions is expected to correspond to low spin configurations Co^{3+} (S = 0) or Co^{4+} (S = 1/2) obtained by filling only the t_{2g} triplet states [29].

The results from χ and ρ measurements imply the phase diagram displayed in Fig. 4. The dominant feature in the *T*-*x* plane is the narrow insulating state at $x = 1/2$, which separates two distinct metallic states. Below $x = 1/2$, we have a ‘‘paramagnetic metal’’ with high conductivity, whereas above $x = 1/2$, there is a ‘‘Curie-Weiss’’ metallic state in which a *T*-linear resistivity coexists with a χ that is Curie-Weiss-like. In contrast, *Yokoi et al*. found that the boundary between the two metals is located approximately at $x = 0.6$. The reason for this discrepancy is not known [30].

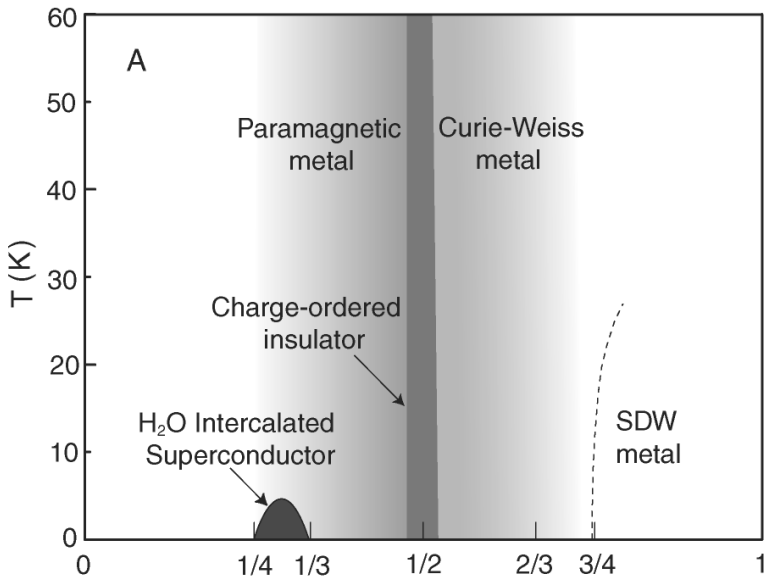

Figure 4. The phase diagram of Na_xCoO_2 in dependence on sodium stoichiometry *x* [29].

In 1997, *Terasaki et al*. studied transport properties of $Na_{0.5}CoO_2$ single crystals and found the highest thermoelectric power to be S = 100 μV/K at room temperature and a comparably low resistivity ρ = 200 $\mu\Omega$cm [19]. The results of their measurements are shown in Figure 5. The resistivity was found to be anisotropic in magnitude and in temperature dependence. The electronic states of layered sodium cobaltate can be considered as quasi 2-dimensional. It shows out-of-plane resistivity with transition from metallic to semiconducting behavior around 190 K with increasing temperature, similar to Sr_2RuO_4 [31].

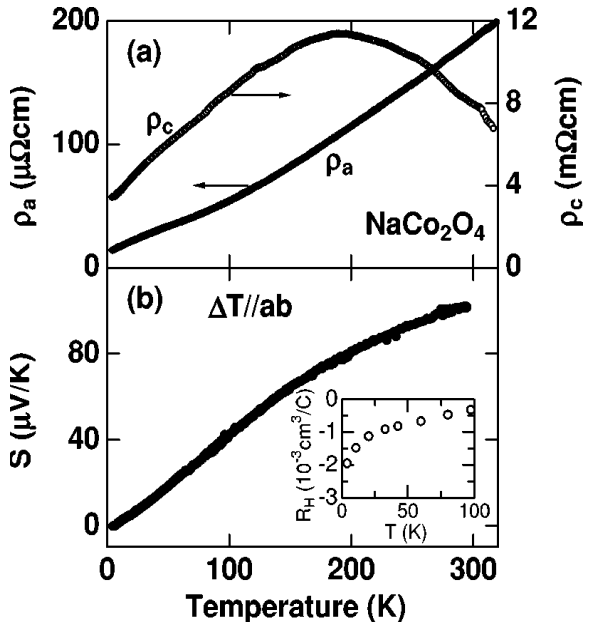

Figure 5. (a) In-plane (ρ_a) and out-of-plane (ρ_c) resistivity of $NaCo_2O_4$ single crystals. (b) In-plane thermoelectric power (S) of $NaCo_2O_4$ single crystal. The inset shows the in-plane Hall coefficient (R_H) of $NaCo_2O_4$ single crystal [19].

Terasaki et al. compared their data with those of Bi_2Te_3, a typical thermoelectric material. The thermoelectric power S of $Na_{0.5}CoO_2$ is only half of that one found in the case of the Bi_2Te_3. Since ρ is only one fifth of that one of Bi_2Te_3, the power factor S^2/ρ is still comparable. However, the mobility 13 cm^2/Vs is more than ten times smaller compared to Bi_2Te_3. This means that $Na_{0.5}CoO_2$ has a much larger number of charge carrier n.

Table 2. Comparison for Na_xCoO_2 and Bi_2Ti_3 parameters, which are related with the thermoelectricity. The values are taken from the paper of *Terasaki et al*. [9].

Parameter	$Na_{0.5}CoO_2$	Bi_2Te_3
ρ [$m\Omega$cm]	0.2	1
$\|S\|$ [$\mu V/K$]	100	200
S^2/ρ [mW/K^{2}cm]	50	40
μ [cm^2/Vs]	13	150

By investigating the thermopower and magnetization in both longitudinal and transverse magnetic field *H*, *Wang et al*. show that Na_xCoO_2 is in fact a strongly correlated system in which the spin entropy term accounts for almost all of Seebeck coefficient at 2 K and a dominant fraction

at 300 K. They report strong dependence of thermopower on magnetic field [17]. The pronounced effect of an in-plane field *H* on *S* is shown in Figure 6. Even at moderately high T (30 K), S decreases significantly in a 14T field. Lowering the temperature makes the field-suppression of *S* more pronounced, until at 4 K, *S* changes sign and saturates near 12 T to a 'floor' value equal to -0.25 μVK^{-2}.With further decrease in *T*, the floor value itself monotonically increases to zero. The trace at 2.5 K shows that S decreases monotonically to zero in a field of 8 T, and remains at zero over an extended field range. The strong effect of field on *S* is also observed with $H \parallel c$ (normal to plane), with the exception that, above 6 K, they observed an additional term that produces an increase in *S* in weak fields. At 4.2 K, *S* displays the same field profile as above, but with a proportionally weaker decrease.

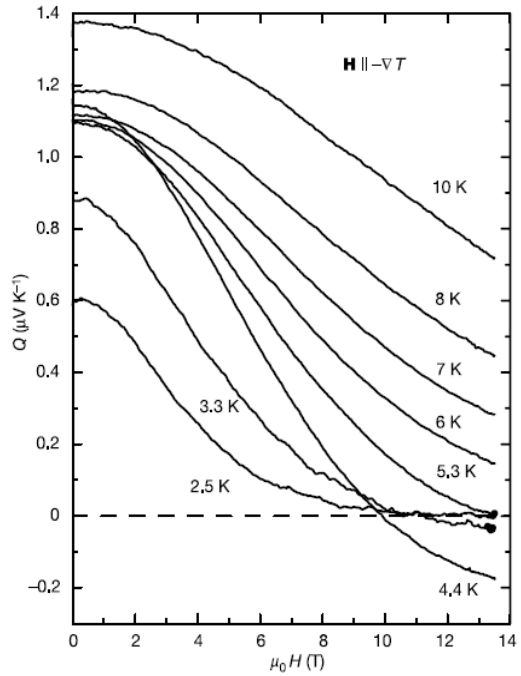

Figure 6. The dependence of in-plane Seebeck coefficient (in this work marked as Q) on in-plane magnetic field *H* measured at the temperature in range 2.5 K to 10 K [17].

Motohashi et al. showed that the thermopower increases with increasing sodium content (Figure 7) which in a local-moment picture corresponds to a progressive dilution of magnetic Co^{4+} (S = 1/2) with nonmagnetic Co^{3+} (S = 0) [32].

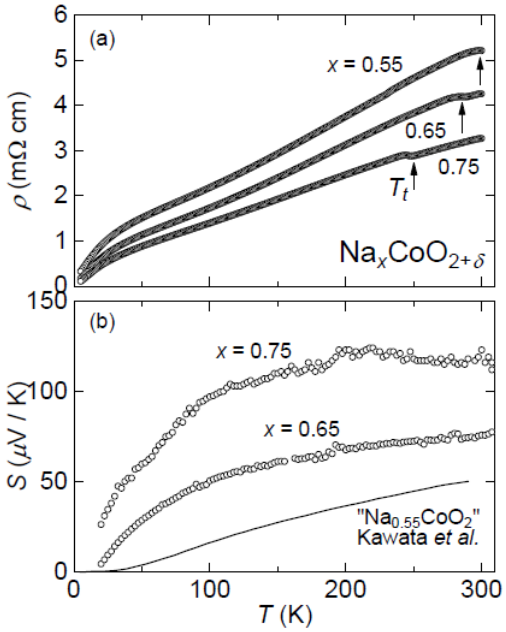

Figure 7. Temperature dependences of ρ and S of $Na_xCoO_{2+\delta}$ samples. The solid curve in (b) represents the previously reported data for $Na_{0.55}CoO_2$ [33].

They also observed a sharp jump at 21.8 K in the dependences of specific heat (*Cp*) on the temperature and hysteresis between zero-field-cooled and field-cooled sweeps below 22 K in magnetic susceptibility measurements on γ- phase Na_xCoO_2 powder samples with $x = 0.75$. This hysteresis increased with decreasing temperature, the maximal concomitant spontaneous magnetization was roughly 10^{-4} μ_B/Co^{4+} site at 2 K. This jump in C_p-T plot represents the magnetic transition temperature (T_m). The curve exhibits a shape typical for the second- order phase transition and the resistivity gradually decreases in the lower temperature region, yielding a kink around T_m in the ρ-T curve. Note that the ρ -T curve has a steeper slope below T_m and decreases toward a very low residual resistivity (ρ_r) of 15 $\mu\Omega$cm. As clearly shown in Fig. 8, all of these anomalies occur at the same temperature [34].

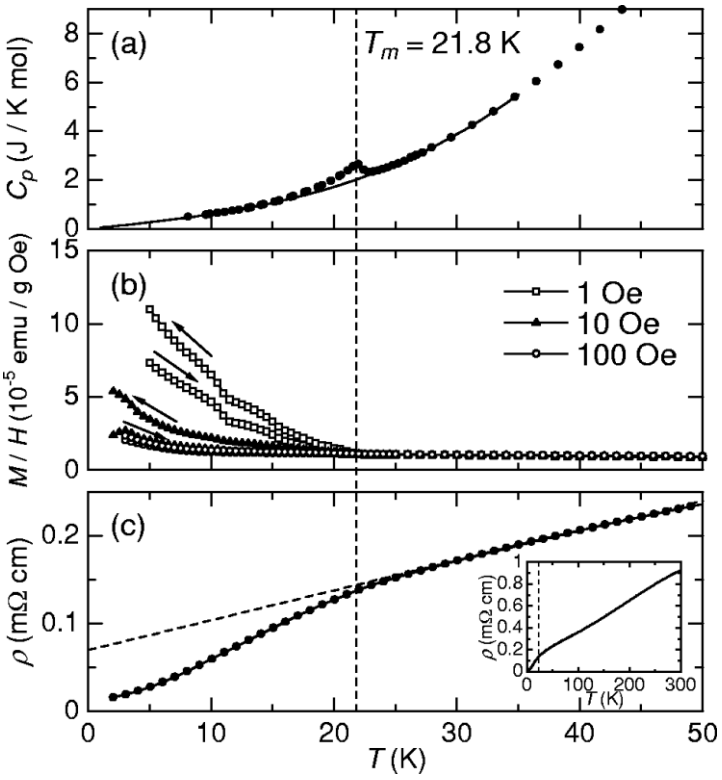

Figure 8. (a) Specific heat *Cp*, (b) magnetic susceptibility *M*/*H*, and (c) electrical resistivity ρ for the $Na_{0.75}CoO_2$ sample with respect to temperature. The inset in (c) shows the ρ -*T* relation for a wider temperature range.

The sodium cobaltate with $x \geq 0.5$ behaves like a Curie-Weiss metal and the magnetic susceptibilities can be described by the Curie-Weiss law. The magnetic susceptibility of single-crystal Na_xCoO_2 shows a strong anisotropy [35]. The magnetic susceptibility $\chi_{\parallel}$ parallel to the *c* direction is smaller than the magnetic susceptibility $\chi_{\perp}$ perpendicular to the *c* direction, [36] [37] and the $\chi_{\perp}$vs $\chi_{\parallel}$ curves show a very good linear relationship in the temperature range of 50- 250 K [38].

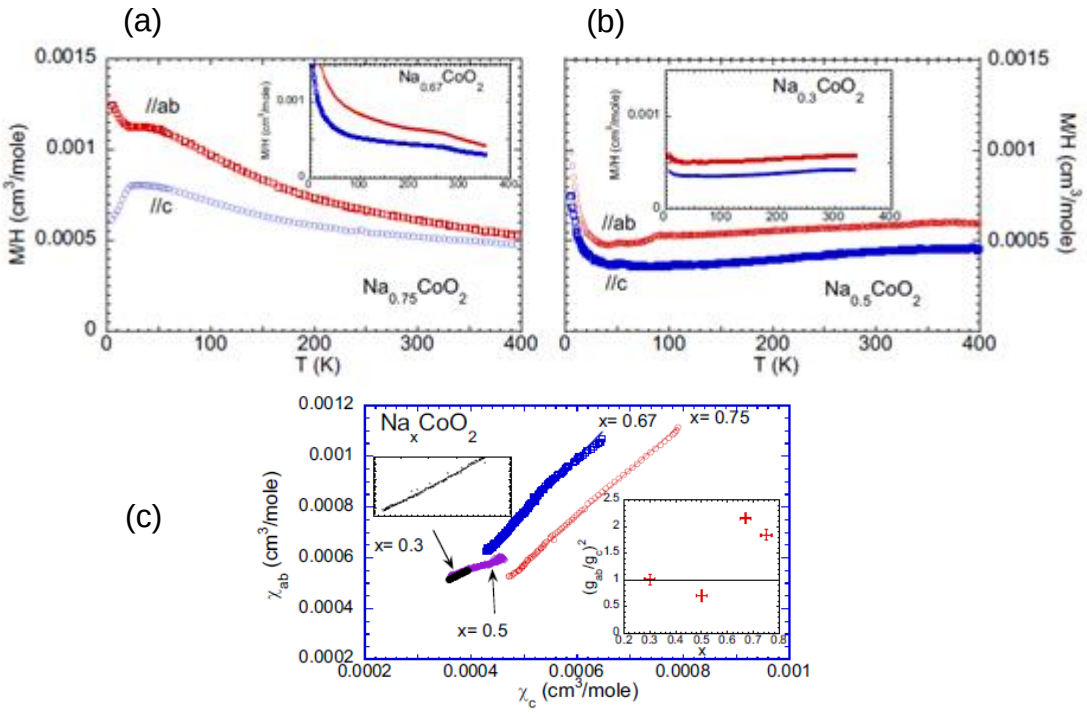

Figure 9. Magnetic susceptibility anisotropy for the Na_xCoO_2 in dependence on magnetic field orientation (a) for $Na_{0.67}CoO_2$ and $Na_{0.75}CoO_2$, (b) $Na_{0.3}CoO_2$ and $Na_{0.5}CoO_2$, (c) The linear relationship for $\chi_{\perp}$ vs $\chi_{\parallel}$.

The Curie constant sharply decreases with the decrease of sodium stoichiometry. It implies, while almost all of Co^{4+} spins are localized for high sodium stoichiometry (x = 75). The fraction of localized spins drops sharply, when Na content is reduced and local moment behavior disappears nearly completely for x = 0.5. The Weiss temperature exhibits significant decrease with the decreasing content of sodium. For the sample with x = 0.75, the Weiss temperature is around −125 K and it suggests the antiferromagnetic correlation between Co^{4+} spins. With the decrease of x to 0.5, decrease of the strength of the antiferromagnetic correlation is observed, which can be described as a transition from localized spin system to delocalized spin one with weaker magnetic coupling [36].

2.3.Synthesis of Na_xCoO_2

The most common synthesis method for preparation of Na_xCoO_2 is a solid state reaction between Co_3O_4 and Na_2CO_3 or Na_2O in the temperature range between 450 °C and 900°C in dependence on stoichiometry and required phase content as showed in phase diagram (Figure 10) published by *Y. Lei et al*. Due to volatility of sodium, up 5 to 10 molar % of sodium excess is commonly used in order to reduce the losses during the annealing [39]. The alternative to the solid state reaction represents soft chemistry method, which provides better mixing on molecular

level [40]. The real sodium content is used to be calculated after synthesis from lattice parameter in direction *c* or it is determined by inductively coupled plasma atomic emission spectroscopy (ICP-AES) or atomic absorption spectroscopy (AAS).

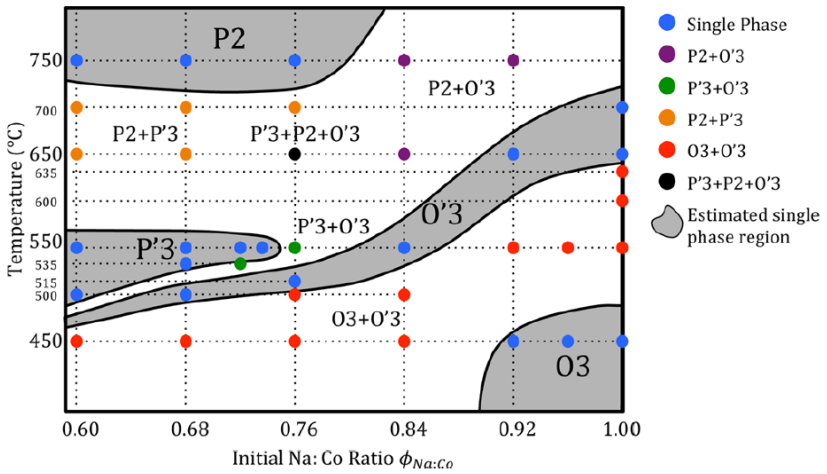

Figure 10. The sodium cobaltate phase diagram in dependence on sodium and annealing temperature revealed by *Y. Lei et al.* [39].

Sodium content after annealing can be controlled by intercalation or deintercalation process. The deintercalation from $Na_{0.7}CoO_2$ to $Na_{0.34}CoO_2$ is reached by stirring of sodium cobaltate in acetonitrile with NO_2PF_6 or Br_2, as oxidizing agent, for two days under inert condition [41] [42]. For softer deintercalation, the stirring with I_2 solution in acetonitrile for several days can be used [42] [43]. The sodium content can be increased by stirring cobaltate in THF with sodium and benzophenone at 95 °C for two days [41], but for intercalation, the use of electrochemical intercalation is more common [28] [39] [45] [46]. The sodium content can be controlled also by solid state reaction of two cobaltates with different sodium stoichiometry [44]. This reaction do not required high temperatures due to high sodium mobility and 200 °C is sufficient temperature.

2.4.Thin films of Na_xCoO_2

Thin films are nowadays established in science as well as in industrial applications as the leading edge of technology. In the case of sodium cobaltates, different deposition techniques have been used, pulsed laser deposition (PLD) [27] [46]- [50], reactive solid phase epitaxy (R-SPE) [51] [54] and sol-gel coating technique [52]. The most studied phase is γ-Na_xCoO_2 but all phases known from bulk form are studied. From the literature, not only variation of deposition technique is known but also wide range of used substrate type, orientation and sodium stoichiometry in the range

between $x = 0.5$ and 0.83. Mostly used single crystal substrate is sapphire Al_2O_3 a- cut [51] or c-cut [46] but also MgO in orientation 001 [27] and 111 [47], $SrTiO_3$ with 001 [27], 110 [48] and 111 [49] orientation, and 001 oriented $LaAlO_3$ have been used [50].

Most studies have been carried out on films prepared by PLD technique. Different deposition condition, sodium content and deposition temperature in the range from 200 to 700 °C were used. The high deposition temperature above 650 °C do not favor formation of Na_xCoO_2 due to high sodium volatility, while the temperatures below 500 °C lead to formation of impurities, such as $Na_2(CoO_3)$, Na_3CoO_2 and Co_3O_4. [53]. The reactive solid phase epitaxy (R-SPE) technique, firstly used by *Ohta et al*. presents suitable way for preparation of γ-Na_xCoO_2 thin films with high sodium stoichiometry ($x = 0.83$). In this work, epitaxial CoO film on *a*–cut sapphire prepared by PLD was transformed to epitaxial Na_xCoO_2 films by reaction with $NaHCO_3$ at 700 °C due to lateral sodium insertion. By this process, the film with thermoelectric properties comparable to bulk was obtained [51].

To the best of our knowledge , just *C. J Liu et al*. used sol-gel technique and spin-coating deposition to produce Na_xCoO_2 thin films with sodium stoichiometry $x = 0.68$. As a sol, the mixture of cobalt and sodium acetate with urea and distilled water was used [52]. The required gamma phase was obtained after annealing at the temperatures of 700- 850 °C and the temperature dependence of thermopower for the γ-Na_xCoO_2 film prepared at 800 °C resembles that of the γ-$Na_{0.68}CoO_2$ film prepared by the reactive solid-phase epitaxy [54], but shows a slightly lower value of ~55 mV/K at 296 K. From XRD measurement, it is known that prepared films content small amount of spinel Co_3O_4 impurities and Na_xCoO_2 films exhibit preferred 001 orientation.

3. Theoretical part

In this chapter, the Pechini process as a process for the preparation of oxide materials are described, then the part dedicated to preparation of thin films follows with the description of chemical solution deposition technique as spin-coating.

3.1. Chemistry of Pechini method

Pechini method is very famous as a simple method for preparing metal oxide powders based on formation of polymeric precursor. The polymeric precursors are made from metal precursors, ethylene glycol and citric acid by low temperature heat-treatment (Figure 11). As a metal precursors, the salts as nitrates, chlorides, carbonates, and acetates are commonly used. This method allows the metal cations to be mixed at a molecular level and the stoichiometric compositions are achieved by chelating the metal ions in solution by citric acid. This process has several advantages in fabrication of ceramic thin films, including low cost, homogeneous compositions, high purity, and low heat-treatment temperatures [55].

Pechini method is based on polymerization of metal citrates using ethylene glycol. A hydrocarboxylic acid such as citric, tartaric and glycolic acids has abilities to form polybasic acid chelates with metal cations in aqueous solutions. Citric acid is more widely used in Pechini processing because of its higher stability. The typical metal complexes with citric ligands tend to be fairly stable due to the strong coordination of the citric ion to the metal cation involving two carboxyl groups and one hydroxyl group. The addition of a glycol such as ethylene glycol leads to the formation of an organic ester. The condensation reaction occurs with the formation of a water molecule, where the hydroxyl group arise from the carboxylic acid and the hydrogen atom from the alcohol. The condensation and polymerization reaction are promoted by heat treatment [56].

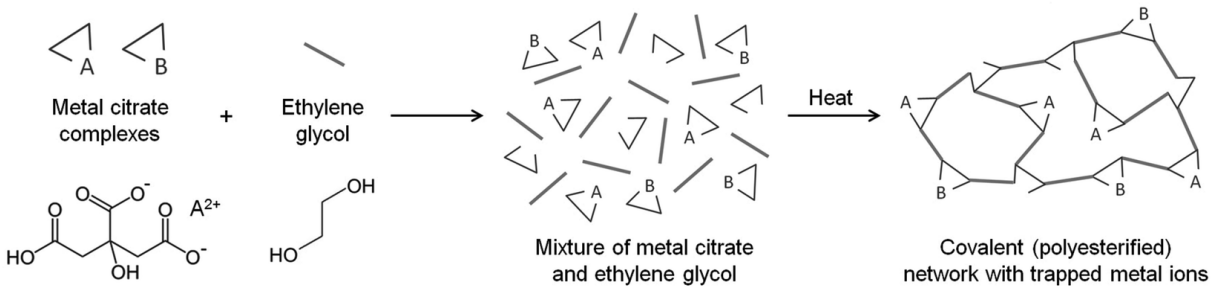

Figure 11. Schematic of the Pechini method of the formation of metal/organic gels [55].

The ratio of complexing agent (EG) to metal cations can be used to control ordering and crystallinity of final product. The ratio of complexing agent (CA) and dispersing agent (EG) affects porosity and particular size of material obtained after calcination. Advantage of Pechini method is that we obtain ceramic precursor with homogenous mixing of reacting metal cations on molecular level after proper pulverization of resin [57] [58].

3.2.Thin film deposition

It is possible to classify the deposition techniques in two ways**Chyba! Nenalezen zdroj odkazů.** [59], physical method and chemical method. The physical deposition procedure consists in vaporization of atoms or molecules from the source material by physical processes such as thermal evaporation or bombardment of the source by an energetic beam of electrons, photons, or ions. The chemical deposition consists in a chemical reaction of vapor or liquid species on the substrate to produce a film of the desired composition.

3.3.Chemical solution deposition (CSD)

The chemical solution deposition technique represents a rapid and cost-effective method for synthesizing high-quality oxide thin films. Thin films are typically formed by spin coating, spray coating or dip coating deposition of precursor on substrate. Desired ceramic phase is subsequently obtained by pyrolysis during heat treatment [60] [61].

In this route, the solution presents a "vehicle" to deposit desired precursors onto substrate. The coating solution is prepared by mixing, and possibly reacting of the individual precursors. The chemical interactions between the starting precursors during deposition solution synthesis depend on the reactivity of the compounds and the preparation conditions. The individual precursor should have sufficient solubility in the solvent and form stable coating solution. The coating solution may be calcinated without undesirable residues during heat treatment. Usually, carboxylates, alkoxides, β-diketons represent the typical suitable starting precursor [61].

Metal carboxylates are salts of carboxylic acids and clearly decompose to metal oxide and gaseous carbon containing products. Carboxylates are normally soluble in their own carboxylic acids, and short alkyl chain salts (i.e., acetate, R = CH_3) are also soluble in water and other highly polar solvents due to their polar nature. Long, non-polar alkyl chains lead to carboxylates (e.g., 2-

ethylhexanoates, R = C_7H_{15}) that are soluble in nonpolar solvents, such as xylene or toluene. Chemically, carboxylates are relatively stable and they are not decomposed by water and oxygen. However, in the case of CSD processing, stability against water means that in the case of carboxylates there is no reaction leading to a gel formation upon addition of water as is the case of metal alkoxides. Due to their polar M–O bond, non-stabilized alkoxides are very sensitive to hydrolysis, leading to the formation of metal hydroxides (M–OH) with the concurrent production of an alcohol molecule:

$$M - OR + H_2O \rightarrow M - OR + ROH$$

If the hydrolysis is rapid, precipitation of hydroxide or oxide/hydroxide species may occur. Alkoxides can be stabilized in order to avoid rapid precipitation after hydrolysis if their organic part R contains further polar groups such as ether linkages, R–O–R′ (e.g., 2-methoxyethanol), amine groups, $–NH_2$, keto groups >C=O, or further alcohol groups, >C–OH.

Prepared coating solution is then deposited on substrate by one of the above mentioned techniques. Typically, for deposition by spin coating, the substrate is held in place on the spinner by applying a vacuum to the backside of the wafer. The wafer is typically wetted by the solution during a ‘static dispense’ using a syringe equipped by filtration unit. The wafer is then accelerated rapidly to1000 to 8000 rpm. The angular velocity and the spinning time, together with the solution viscosity and concentration, can be used in order to control the thickness of the wet film and then the thickness of the final ceramic film.

In order to obtain the desired oxide phase, solvent remaining entrapped within the pore structure of the film and the organic moieties associated with the gel network must be removed. Typically, the oxide phase is obtained by heat treatment. The calcinated inorganic material is very porous because the large fraction of the precursor volume is eliminated during pyrolysis as volatile hydrocarbon gases or water vapor or both. This volume reduction during evaporation and pyrolysis lead to the formation of cracks. This can be reduced by producing of thinner precursor films with the thickness less than critical value and final film thickness is built up using several repetition of coating and pyrolysis steps.

The transformation of the as-deposited film into the crystalline ceramic can be described as *two-step* or *one-step process*. In the *two-step process*, the removal of the organic constituents is

carried out in a separate processing step (i.e., the first stage of the two step method) at lower temperatures (200 – 400°C) prior to a high-temperature crystallization step. In the *one-step process*, organic removal and crystallization are accomplished in the same processing step, which is carried out at temperatures sufficiently high to induce crystallization of the oxide. It leads to the different nucleation processes. The higher crystallization temperatures lead to increased densification and larger grains. This is due to the temperature-activated mobility of the ions.

3.4.Epitaxial grain growth

Control of nucleation at the substrate – film interface can be used for the preparation of epitaxial and highly oriented (textured) films. The nucleation at higher temperatures implies that the crystallization process occurs with a lower driving force. This causes heterogeneous nucleation at the substrate to become more important in defining film microstructure, which may favor the production of films with a higher degree of orientation [60] [61].

For the case where only nucleation at the substrate interface occurs, crystallographic growth along fast growth directions can results in highly oriented films. The transformation from the amorphous state to the crystalline state is completely associated with the grains nucleated at the substrate.

The crystallographic structure of the substrate may also play a role in the preparation of oriented films. The decrease of energy barriers for homogenous and heterogeneous nucleation is expected for the substrates and the film with a higher degree of lattice matching and the heterogeneous nucleation at the substrate to become more preferred than other nucleation events.

In addition, the changes in precursor chemistry led to a change in the characteristics of the calcinated film, which affected the nucleation and the growth behavior. Epitaxial grain growth occurs when the film and substrate have identical structures and small lattice mismatch. In contrast, the growth of oriented thin films on substrates with different structure is due to morphological instability phenomena and abnormal grain growth. If the grain size exceeds the film thickness, grains with specific orientations will undergo abnormal grain growth due to their lower surface and energy of interface.

Depending on lattice matching and structural differences between the film and substrate, the fabrication of epitaxial films proceeds according to four different phenomena. The *epitaxial film growth* is observed for materials that display good lattice matching. The difference in lattice

constants is less than a few percent. The development of epitaxial films involves the growth of small, nanometer-sized grains at the substrate - film interface. The grains eventually grow along the interface and then through the film to "consume" randomly oriented grains. In the case when the film and substrate have different structures or surface area, the mismatches are observed in the *Two-step processing*. In this case, the epitaxy is achieved through a two-step process where a polycrystalline film is first deposited, and then heated leading to break-up into isolated seeds grains that possess a low interfacial energy. Onto this surface, a thick film is subsequently deposited, and the isolated islands act as nucleation sites (seeds) for the growth of a highly oriented film. When higher processing temperatures are employed, epitaxial films may also be formed via a liquid phase. This is called *Liquid phase processing.* If low precursors concentrations in the coating solution are used, in conjunction with heat treatment of each individual layer, it can emphasize heterogeneous epitaxial growth and suppress nucleation within the film. This is called *One-step processing*.

3.5.Introduction to thermal and electric transport

In this chapter, the non-equilibrium thermodynamic and the Boltzmann transport theory is used for the introduction of thermal and electric transport in solid state. The outline of this section generally follows the *Terasaki´*s work [9].

3.5.1. Inequilibrium thermodynamic

Quite generally, the electric current density **j** (charged particle flow) and the thermal current density **q** are written as functions of the gradient of chemical potential $\nabla\mu$ and the gradient of temperature $\nabla(1/T)$ as

$$-\mathbf{j} = L_{11}\frac{1}{T}\nabla\mu + L_{12}\nabla\frac{1}{T}$$

$$\mathbf{q} = L_{21}\frac{1}{T}\nabla\mu + L_{22}\nabla\frac{1}{T}$$

where L_{ij} are transport parameters (Callen 1985). The chemical potential consists of an electrostatic part $\mu_e = eV$ and a chemical part μ_c. Then the electric field is given as:

$$\mathbf{E} = -\nabla V = -\frac{1}{e}\nabla(\mu - \mu_c)$$

However, $\nabla\mu_c$ cannot be observed separately in real experiments, and is considered to be included in the observed **E** hereafter (Ashcroft and Mermin 1976). Then the above equations are identical to the Boltzmann transport equations given as:

$$\mathbf{j} = \sigma\mathbf{E} + S\sigma\nabla(-T) \quad (1)$$

$$\mathbf{q} = ST\sigma\mathbf{E} + \kappa'\nabla(-T)$$

where σ the conductivity, and κ' is the thermal conductivity for $\boldsymbol{j} \neq 0$. Then, for $\nabla T = 0$, we can eliminate the electric field term from Eqs and obtain:

$$\frac{\mathbf{q}}{T} = S\mathbf{j}$$

Since the left hand side is the entropy current density, we can say that the thermopower S is equivalent to the ratio of the entropy current to the electric current, or is equivalent to entropy per carrier.

3.5.2. Boltzmann transport theory

One-electron states in a periodic potential are exactly solved, and the solution is known as the Bloch function. The Bloch function has a wave number **k** (crystal momentum) as a well-defined quantum number, and its energy $\varepsilon = \varepsilon(\mathbf{k})$ is written as a function of **k** (band dispersion relation).

To recover a particle picture, we make a wave packet from the Bloch functions. Then the velocity of the particle is given as the group velocity of the wave as

$$\mathbf{v}_k = \frac{1}{\hbar}\nabla_k\varepsilon(\mathbf{k}) = \frac{1}{\hbar}\left(\frac{\partial\varepsilon}{\partial k_x} + \frac{\partial\varepsilon}{\partial k_y} + \frac{\partial\varepsilon}{\partial k_z}\right)$$

To keep the particle picture, every wave constituting the wave packet should satisfy the relation of $\hbar\mathbf{k} = m\mathbf{v}_k$with a constant value of *m*. Then we get $m\nabla\mathbf{v}_k = \hbar\nabla\mathbf{k}$, and the effective mass (the inverse of the effective mass tensor) in a solid is given as

$$\frac{1}{m_{ij}} = \frac{1}{\hbar}\frac{\partial v_{ki}}{\partial k_j} = \frac{1}{\hbar^2}\frac{\partial^2\varepsilon}{\partial k_i\partial k_j}$$

Thus the electron in a solid behaves like a charged particle with the charge *e*, the mass *m* and the velocity $\mathbf{v}_k$. Since electrons are fermions, they obey the Fermi-Dirac distribution f_0. Then the electric current density and the thermal current density are written as

$$\mathbf{j} = \frac{1}{4\pi^3}\int e\mathbf{v}_k f_k d^3k$$

$$\mathbf{q} = \frac{1}{4\pi^3}\int e(\varepsilon(\mathbf{k}) - \mu)\,\mathbf{v}_k f_k d^3k$$

where f_k is the distribution function at an non-equilibrium state and is given as a solution of the Boltzmann equation written as:

$$\mathbf{v}_k \cdot \nabla f_k + \frac{e}{\hbar} E \cdot \nabla_k f_k = \left.\frac{\partial f_k}{\partial t}\right|_{scattering}$$

where the right side is the scattering term. In the case of weak perturbation, we can linearize *f* as $f_k = f_0 + g_k$. We further assume the relaxation-time approximation to introduce the relaxation time τ as

$$-\frac{1}{\tau} g_k = \left.\frac{\partial f_k}{\partial t}\right|_{scattering}$$

Eventually we get $g_k = \left(-\frac{\partial f_0}{\partial \varepsilon}\right)_{\varepsilon(k)=\varepsilon} \mathbf{v}_k \tau \left\{eE + \frac{\varepsilon(\mathbf{k})-\mu}{T}(-\nabla T)\right\}$ and by substitution this to the Eqs. for j and q we obtain $\mathbf{j} = e^2 K_0 \mathbf{E} + \frac{e}{T} K_1 (-\nabla T)$ and $\mathbf{Q} = eK_1 \mathbf{E} + \frac{e}{T} K_2 (-\nabla T)$ where K_n is a second rank tensor through $\mathbf{v}_k \mathbf{v}_k$ in general

$$K_n = \frac{1}{4\pi^3} \int \left(-\frac{\partial f_0}{\partial \varepsilon}\right)_{\varepsilon(k)=\varepsilon} \mathbf{v}_k \mathbf{v}_k \, \tau (\varepsilon(\mathbf{k}) - \mu)^n d^3k$$

The conductivity and thermopower is given as:

$$\sigma = e^2 K_0 = \frac{e^2}{4\pi^3} \int \left(-\frac{\partial f_0}{\partial \varepsilon}\right)_{\varepsilon(k)=\varepsilon} {\mathbf{v}_k}^2 \, \tau (\varepsilon(\mathbf{k}) - \mu) d^3k$$

$$S = \frac{1}{eT}\frac{K_1}{K_0} = \frac{1}{eT} \frac{\int \left(-\frac{\partial f_0}{\partial \varepsilon}\right)_{\varepsilon(k)=\varepsilon} {\mathbf{v}_k}^2 \, \tau (\varepsilon(\mathbf{k}) - \mu) d^3k}{\int \left(-\frac{\partial f_0}{\partial \varepsilon}\right)_{\varepsilon(k)=\varepsilon} {\mathbf{v}_k}^2 \, \tau d^3k}$$

The thermal conductivity is given as $\kappa' = \frac{K_2}{T}$.

4. Aim and motivation

The aim of this work can be divided into two main directions. The first goal concerns bulk materials, where we will focus on the study of thermoelectric and magnetic properties of layered cobaltate Na_xCoO_2 in dependence of structure and sodium stoichiometry. We will look for the differences of thermoelectric and magnetic properties of α- and γ-phases. The second goal is to prepare the γ-phase in thin films formed by chemical solution deposition method using the spin-coating deposition technique and study stability and decomposition of Na_xCoO_2 in the dependence of sodium content.

Many experimental studies on Na_xCoO_2 have been done and there are several working group, which are focused on the study of layered cobaltates, but the results are not always consistent. For this reason, we think that there is still place to bring more clarity in this research field. Our attention is dedicated on thin film formation by CSD because it is known from literature review that many works was done in this field especially on films prepared by PLD, but to the best of our knowledge, the preparation of Na_xCoO_2 by CSD is reported only in the work of *C. J. Liu et al*.

5. Experimental part

This chapter is divided into three parts. In the first part, the synthesis of ceramic Na_xCoO_2 samples with sodium stoichiometry x = 0.70, 0.80, 0.90, and 1.00 by Pechini method is described. The second part describes the preparation of Na_xCoO_2 thin films by CSD method. The last part summarizes the experimental conditions of experimental measurements.

5.1. Synthesis of Na_xCoO_2 ceramic

Sodium cobaltate was prepared by soft chemistry method described in the works of *Lone-Wen Tai* [57] [58]. For a typical synthesis of 10.0 g of Na_xCoO_2, the appropriate amount of $Co(NO_3)_2.6H_2O$, Na_2CO_3, citric acid (CA) and ethylenglycol (EG) was dissolved in 130 ml of distillated water and 20 ml of concentrated HNO_3. The molar ratio of n(Na)/n(Co) depends on required stoichiometry Na_xCoO_2 (x = 0.75, 0.80, 0.90, 1.00). The Table 3 summarized the amounts of single reactants. Prepared mixture was heated up on heat plate in 1.5 L beakers to reduce the solvent volume and to initiate the polymerization. When viscous fluid started to increase the volume, the beaker was replaced to the furnace preheated to 150 °C. After 5 hours dry porous resin was obtained, which was properly grounded in mortar. The grounded resin was then progressively heat treated at 300°C for 24 hours and then 48 hours at the temperature of 550 °C to remove organic phase. After that, the powdered samples were pressed into pellets suitable for thermoelectric measurements.

Table 3. The summary of prepared powder samples and weights of precursors. Symbol T in the sample labels represent annealing temperature.

Sample label	Sample stoichiometry	$Co(NO_3)_2.7H_2O$		Na_2CO_3		CA	EG
		m [g]	n [mol]	m[g]	n [mmol]	n [mmol]	n [mmol]
NCO_0.7/T	$Na_{0,7}CoO_2$	29.913	0.103	3.813	36.0	175.0	151
NCO_0.8/T	$Na_{0,8}CoO_2$	27.953	0.096	4.071	38.4	172.8	149
NCO_0.9/T	$Na_{0,9}CoO_2$	26.302	0.090	4.311	40.7	171.4	148
NCO_1.0/T	$Na_{1,0}CoO_2$	28.109	0.097	5.117	48.3	193.6	167

The pellets were firstly annealed at the temperature of 600 °C, and then gradually heat treated at 650°C, 700°C and 750°C. The heating cycle started at the room temperature and reached the final temperature with heating rate of 5 °C per minute. At required temperature, the samples were annealed for 120 hours. After annealing, the samples were cooled down to room temperature with the rate of 1°C per minute. The heating cycles for all temperatures is described in detail in Table 4.

Table 4. Summarization of heat treatment steps for samples. The symbol x in the sample name represent sodium stoichiometry.

Sample	Annealing 1	Annealing 2	Annealing 3	Annealing 4
NCO_x/600	120 h/600 °C			
NCO_x/650	120 h/600 °C	120 h/650 °C		
NCO_x/700	120 h/600 °C	120 h/650 °C	120 h/700 °C	
NCO_x/750	120 h/600 °C	120 h/650 °C	120 h/700 °C	120 h/750 °C

5.2.Preparation of Na_xCoO_2 thin films

Thin films of Na_xCoO_2 were prepared by CSD (chemical solution deposition). The coating solutions were prepared from the solution of Cobalt(II) 2-ethylhexanoate [$Co(ehex)_2$] in mineral spirit and from in-situ generated sodium isobutoxide. 2,2-diethanolamine (DEA) was used as modifier. The coating solutions have standard Co concentration c = 0.33 mol.dm^{-3}. The molar ratio of n(Na)/n(Co) depends on required stoichiometry (x = 0.0, 0.175, 0.35, 0.52, and 1.0). The molar ratio modifier-to sodium was n(DEA)/n(Na)= 2. Table 5 summarized composition of deposited solutions used in this work. For preparation of seed layers, diluted solutions with Co concentration c = 0.165 mol.dm^{-3} were used.

Table 5. The Summary of used coating solution.

Coating solution	Na		$Co(ehex)_2$; w = 0.65	
	m [g]	[mmol]	m [g]	n [mmol]
NCO_1.0	0.621	27.0	14.35	27.0
NCO_0.52	0.471	20.4	20.93	39.4
NCO_0.35	0.422	18.4	27.86	52.4
NCO_0.175	0.253	11.0	33.41	62.8
Co_xO_y	-		15.0	28.2

The coating solutions were deposited on polished substrates by spin-coating using the coater RC8 Gyrset, KarlSuss. Substrates (00l oriented α-Al_2O_3) were firstly cleaned by sonication in acetone solution for 15 minutes and then by treatment with plasma Zepto, Diener electronic, Germany. Were used two different deposition conditions. For seeding cycle diluted sol was used and the spinning velocity was of 4000 rpm**.** Rotation time was 40 seconds. After drying at 110 °C for 10 minutes, the sample were rapidly heated to 300 °C and calcined for 5 minutes. After drying, the films were annealed at required temperature for 30 minutes at preheated tubular furnace. For deposition of bulk Na_xCoO_2 films, solutions with standard Co concentrations were used, the spinning velocity and spinning time was 3000 rpm and 40 seconds, respectively. For drying and calcinations, the same conditions as in seeding cycle were used. The annealing time was shortened to 10 minutes. Required films thickness were obtained by repeating of deposition cycle. To prevent decomposition of Na_xCoO_2 films caused by sodium loses due to its reaction with substrate, the approach of reactive solid phase epitaxy (R-SPE) was used and samples were annealed in Na_2CO_3 capsules.

5.3.Characterization methods

5.3.1. Powder X-ray diffraction

Ceramic samples measurements were carried out on PANalytical X´pert Pro diffractometer using Cu $K_{\alpha 1,2}$ radiation with secondary graphite monochromator and PIXcel detector. Structure refinement was provide by Rietveld method in Fullprof software package [62]. Samples were measured from 10 °2Theta to 100 °2Theta with the step of 0.013 °2Theta. The texture characterization and pole figure measurements of thin films were done using PANalyticalX'Pert MRD diffractometer (Cu $K_{\alpha 1,\ 2}$ radiation, polycapillary in the primary beam, Eulerian cradle, parallel-plate collimator and secondary monochromator).

5.3.2. Elementary analysis

The molar ratio of *n*(Na)/*n*(Co) in the samples were determined by atomic absorption spectroscopy (AAS) in IIC. The AAS was measured on Avanta E by GBC Company equipped with acetylene- oxygen burner. The cobalt concentration was determined in absorption and sodium in emission mode. Cobalt nitrate was used as a standard for calibration solution, which concentration

was determined by chelatometry titration. As a sodium standard, dried sodium chloride was used. The concentrations of calibration solutions was in the range of 0 to 50 ppm. Solid samples of Na_xCoO_2 for AAS analysis were dissolved in concentrated HCl and then the stock solution with concentration, which correspond to calibration curve (ca. 25 ppm Co), were prepared.

5.3.3. Measurements of transport properties

Transport properties, *i.e.* electrical resistivity, thermoelectric power (Seebeck coefficient) and thermal conductivity measurements, were carried out in Institute of Physics of the CAS at the Laboratory of oxide materials using home-build system within the temperature range of $3.5\ K < T < 310\ K$. The low temperature cell construction and the sample arrangement are shown in Fig. 12.

The four point steady-state method with separated measuring and power contacts (sample extremities) was applied to eliminate the thermal resistances between the sink and the heater, respectively. The rectangular-shaped sample was mounted on the heat sink of cryostat and the miniature resistor heater, charged using a pair of 0.003 in. chromel wires, was stuck by general electric (GE) varnish on the end of the sample. A thin isolating paper (cigarette paper) is placed between the heater and the sample to avoid the electrical current transfer from the heater to the sample and simultaneously ensured that its small thickness is not blocking the thermal transfer.

The temperature gradient and voltage drop was monitored using two separated differential chromel-constantan thermocouples (0.003 in. in diameter) which were affixed to the sample using copper link, indium solder, and silver paint. Four Cu contacts with a low electrical resistivity and a high thermal conductivity are attached to the sample, placed in a special cell. Ag paste is placed between Cu contacts and the sample to obtain a better electrical and thermal energy transport. The inner Cu contacts are for the connection of differential E-type thermocouples made from chromel to measure ΔT. The outer Cu contacts are for the input and output of electrical current. The lower part of the cell is made by Cu and is attached to the recycling cryostate by thermal paste (Apiezon) for better thermal contact.

The electrical current density varied depending on the sample resistivity between 10^{-1} Acm^{-2} (metallic state) and 10^{-7} A cm^{-2} (insulating state).

A typical temperature difference applied across the sample was 1.5 K. The influences of the thermopower of chromel, in case of thermovoltage measurement, and sample radiation, and thermal conductivity of differential thermocouples, in case of thermal conductivity measurement, were carefully taken into account and corresponding corrections were made. The experimental setup was checked using reference samples (superconducting Bi-2223 ceramics, chromel, plexiglass, . . .) and the error within all range of temperatures did not exceed absolutely ~1 μV K^{-1} (thermopower) and ~0.1 W m^{-1} K^{-1} (thermal conductivity) or relatively of 5% of measured value.

The Seebeck coefficient has to be corrected due to the influence of the chromel thermocouples ($S_{chromel}$) by the relation:

$$S = \frac{\Delta V}{\Delta T} + S_{chromel}$$

The thermal conductivity is calculated as:

$$\kappa = \frac{P}{\Delta T}\frac{L}{A}$$

where P is the heater power, ΔT is the temperature difference between the inner Cu contacts and A is the cross-section area of the sample. The correction of the heater and the sample radiation and the additional thermal transport through the Cu contacts is applied.

The measurement itself is taking place in a recycling cryostat and the system reaches the vacuum to 10-3 Pa by rotary oil pump and the pressure of 10-6 Pa is reached by using a turbomolecular pump. Such a low pressure is necessary to avoid the condensation of atmospheric gases and water

The constant temperature and minimization of thermal losses is required for each step of measurement. Therefore the low temperature cell is covered by a Cu hood with a mass of ~ 300 g and high heat capacities which ensure the constant temperature at each measurement step. An additional dural hood covering the Cu hoot ensures that radiation losses are minimized.

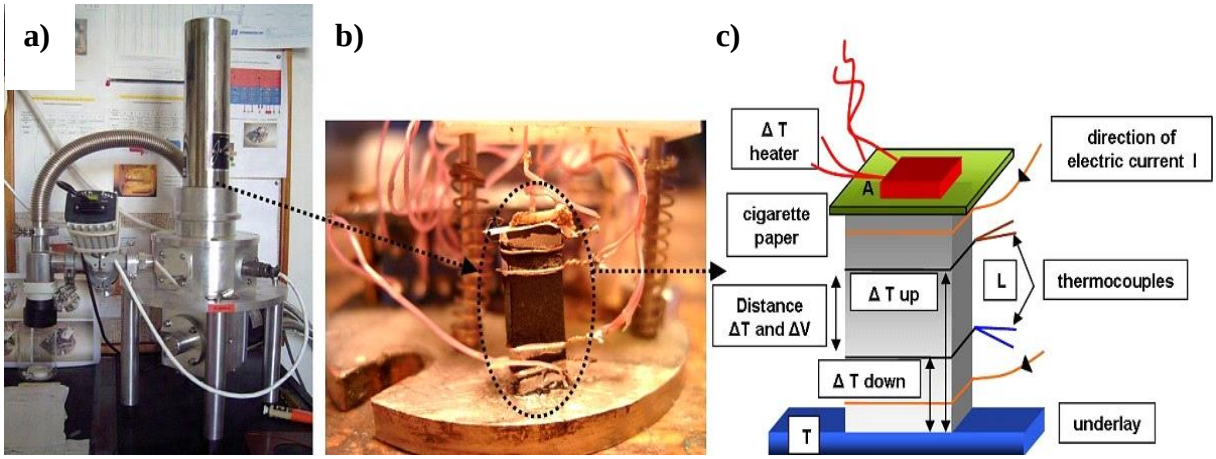

Figure 12. (a) A home-made system with recycling cryostat for the Seebeck coefficient, thermal conductivity and electrical resistivity measurements, (b) detail of a low temperature cell, and (c) sketch showing the sample arrangement for the measurement.

The calculations of Seebeck coefficients were made with the WIEN2K program [63]. This program is based on the density functional theory (DFT) and uses the full-potential linearized augmented plane-wave (FP LAPW) method with the dual basis set. In the LAPW methods, the space is divided into atomic spheres and the interstitial region. The electron states are then classified as the core states that are fully contained in the atomic spheres and the valence states. The valence states are expanded using the basis functions; each of the basis functions has the form of the plane wave in the interstitial region, while it is an atomic-like function in the atom spheres. The core states were defined as electronic configuration (Ne, $3s^2$) for Co, and as (He) for Na and O atoms. The radii of the atomic spheres were taken 2.3 a.u. for Na, 1.9 a.u. for Co and 1.6 a.u. for O. The number of *k* points in the irreducible part of the Brillouin zone was 320. The calculation of the Seebeck coefficients was done within Boltzmann transport theory using the BOLTZTRAP package [64] under the constant relaxation-time approximation for the charge carriers.

5.3.4. Measurements of magnetic properties

The magnetic susceptibility was measured in Institute of Physics of the CAS at Laboratory of oxide materials using a SQUID magnetometer MPMS-5S (Quantum Design) in the temperature range of 4 K < *T* < 350 K. The measurements were performed applying a field of 0.1 T on zero field-cooled (ZFC) and on field-cooled (FC) samples.

5.3.5. Microstructure analysis

The microstructure analysis of the thin films were carried out by a scanning electron microscope (SEM) and by an atomic force microscope (AFM). The SEM analysis was provide in Brno by JEOL JSM-6510lv equipped with field emission gun. The AFM measurement was carried out in IIC in Rež by Bruker Icon Dimension scanasyst.

6. Result and discussion

In this chapter, the result for ceramic bulk samples and thin films are summarized and discussed. The results of the bulk samples are divided by the used experimental methods on PXRD analysis, AAS analysis, the Seebeck coefficient measurement and magnetic susceptibility. The second chapter is dedicated to the thin films results.

6.1.PXRD analysis

The results in this chapter are dedicated to the qualitative and the quantitative PXRD analysis. The quantitative and the structure analysis were carried out by Rietveld refinement and shows the progress of phase composition with the rising of annealing temperature.

The PXRD data of NCO_0.7 samples after annealing are presented in fig. 13a. The dependence of phase composition of NCO_0.7 sample on the annealing temperature is showed in Figure 13b. Figure 14a and b showed same data for NCO_0.8, fig. 15 for NCO_0.9, and fig. 16 for samples NCO_1.0.

The calcination at the temperate of 550°C leads to the crystallization of rhombohedral *R-3m* sodium cobaltate phase and cobalt spinel Co_3O_4. Molar ratio between cobalt spinel and layered phase depends on sample stoichiometry and the sample NCO_0.7/550 exhibits the highest spinel content 78 molar % of $CoO_{4/3}$, see (fig.13a) (when expressing molar ratios, we use a formula $CoO_{4/3}$, instead of Co_3O_4 for better comparison of Co amount in respective phases). The spinel content decreases with higher sodium content and the sample NCO_1.0/550 contains 60 molar % of $CoO_{4/3}$. After annealing at the temperature of 600 °C, we obtained almost pure rhombohedral *R-3m* sodium cobaltate phase for all samples, except for the sample NCO_0.7/600 (Figure 13a), where we still observed the spinel diffraction in the diffraction pattern. The susceptibility measurement, which is more sensitive to Co_3O_4 than PXRD (see section 6.4.), later revealed the presence of Co_3O_4 impurity in all samples annealed at 600°C in the amount of 1-3 molar%. The crystallization of the hexagonal *$P6_3/mmc$* sodium cobalt phase was observed after annealing at 650 °C. These samples represent the mixture of rhombohedral and hexagonal phases without other impurities. The rhombohedral phase is presented just as minority phase (about 10 molar%) after annealing at the temperature of 700 °C. The samples heat-treated at 750 °C are formed from pure hexagonal phases with Na_2CO_3 impurities. The amount of Na_2CO_3 drops with sodium reactant

content, so that finally the sample NCO_0.7/750 contains Co_3O_4 impurity instead of Na_2CO_3, in agreement with susceptibility data.

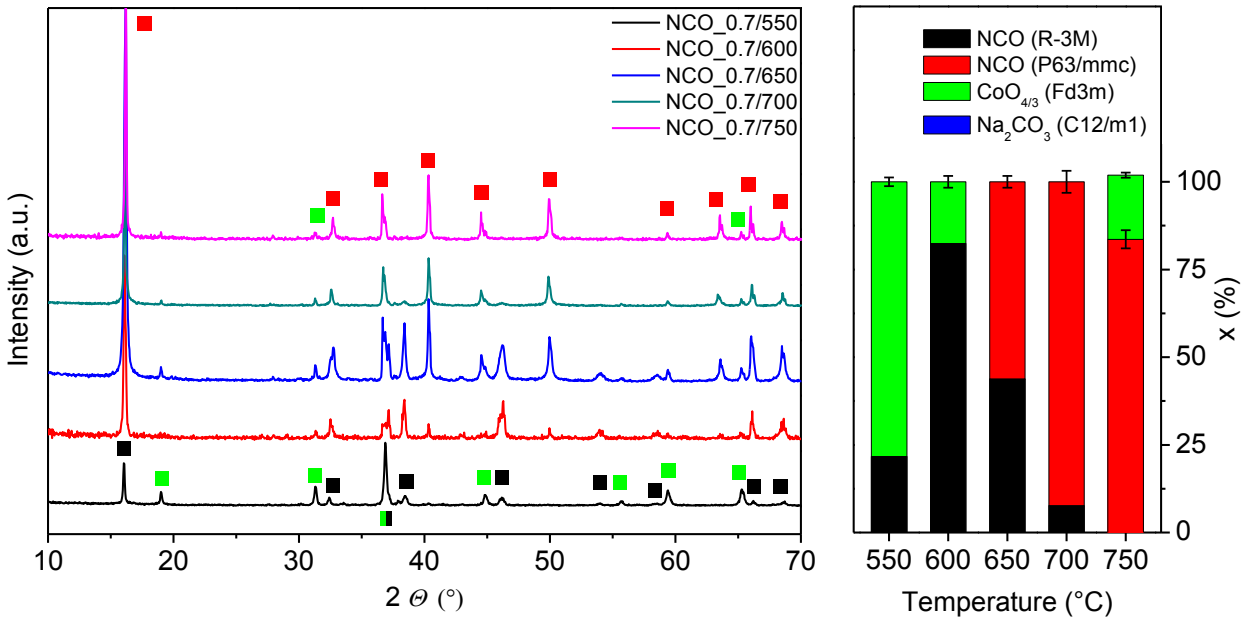

Figure 13. (a) Diffraction patterns of the sample NCO_0.7 annealed in the temperature range from 550 °C to 750 °C. (b) The dependence of phase composition on the annealing temperature for NCO_0.7.

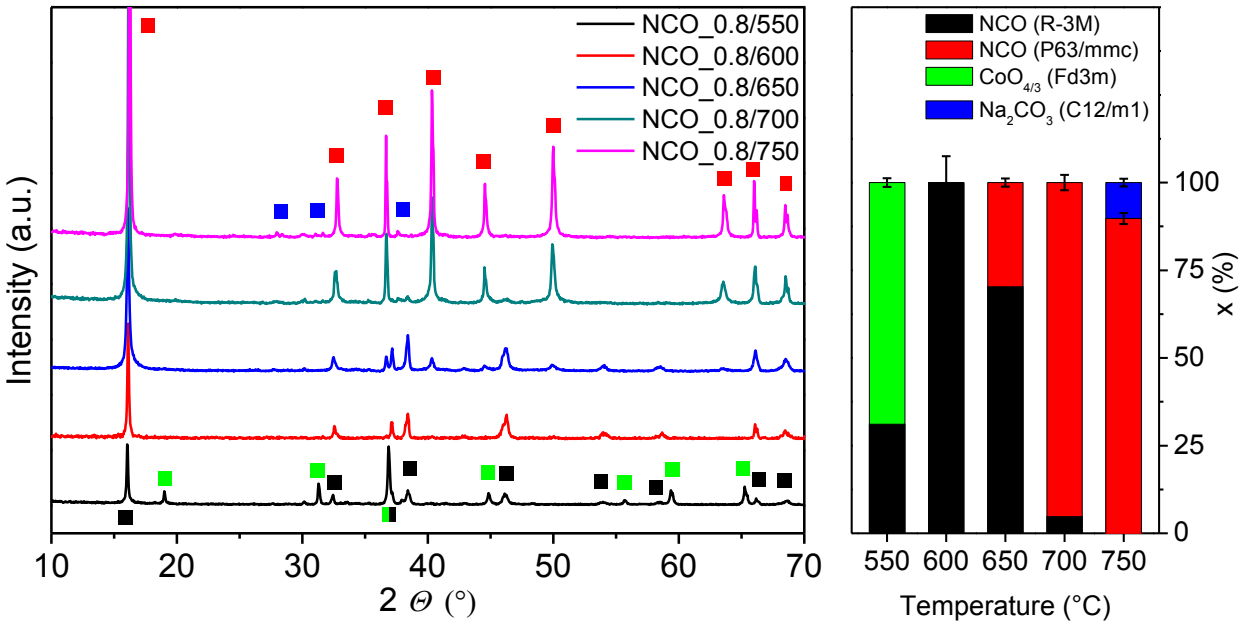

Figure 14. (a) Diffraction patterns of the sample NCO_0.8 annealed in the temperature range from 550 °C to 750 °C. (b) The dependence of phase composition on the annealing temperature for NCO_0.8.

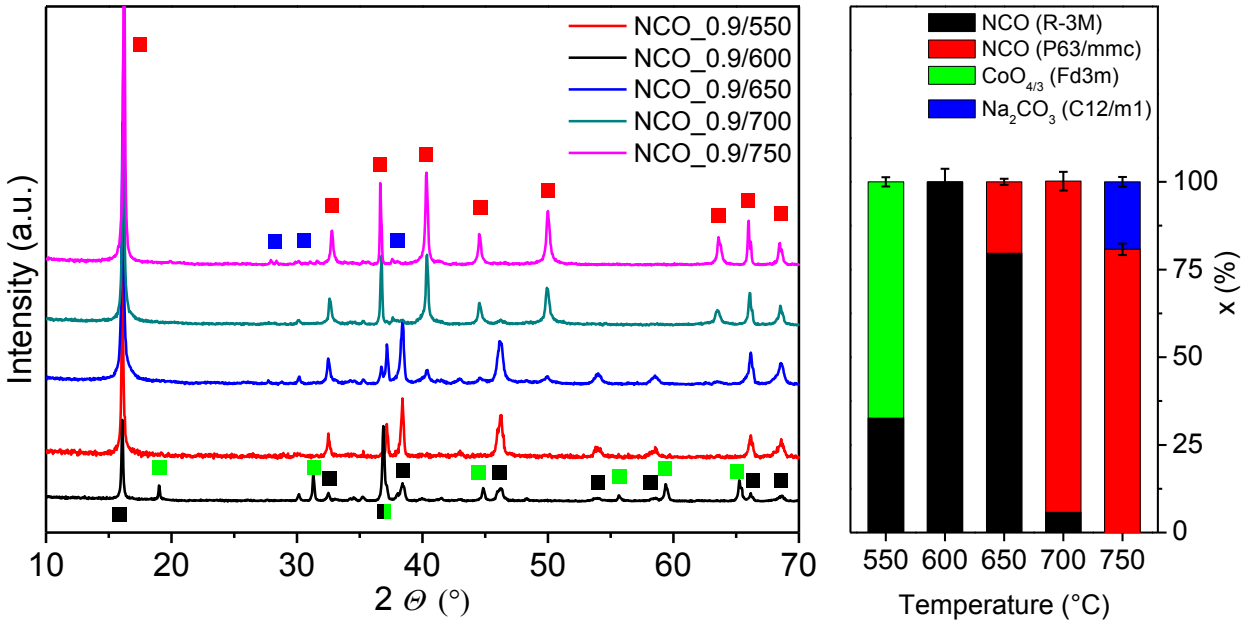

Figure 15. (a) Diffraction patterns of the sample NCO_0.9 annealed in the temperature range from 550 °C to 750 °C. (b) The dependence of phase composition on the annealing temperature for NCO_0.9.

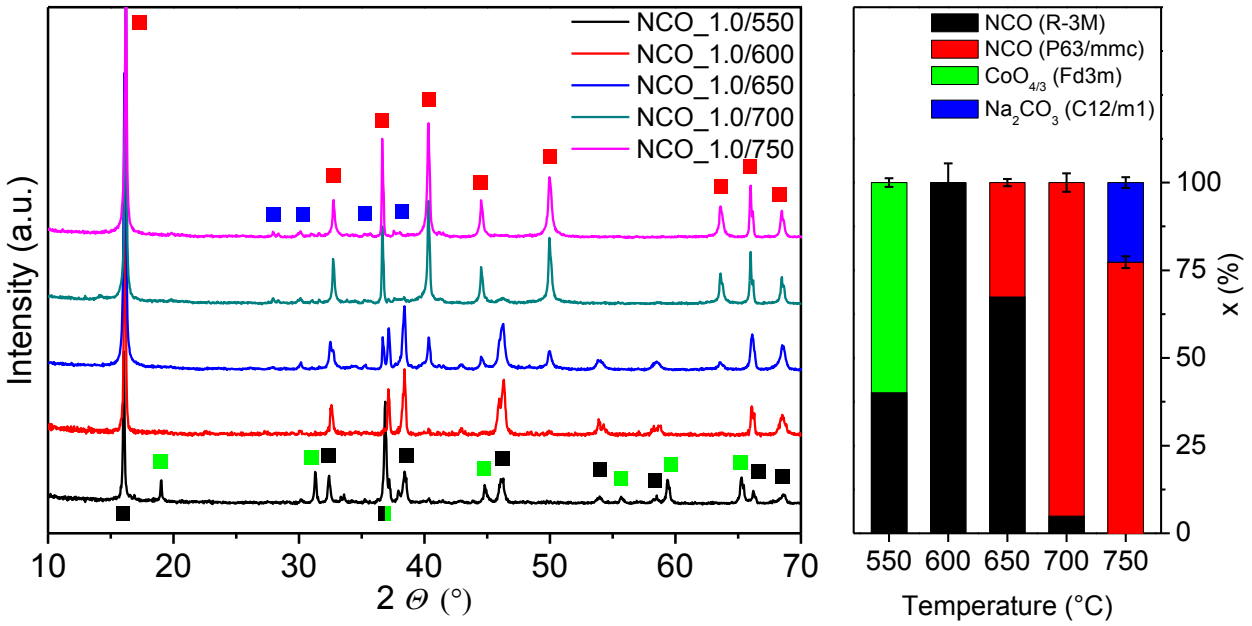

Figure 16. (a) Diffraction patterns of the sample NCO_1.0 annealed in the temperature range from 550 °C to 750 °C. (b) The dependence of phase composition on the annealing temperature for NCO_1.0.

Figure 17. shows dependence of lattice parameter *c* determined by Rietveld refinement on the annealing temperature and the corresponding sodium stoichiometry, extracted from the linear dependence of lattice parameter *c* on sodium content[28] [41]. Figure 17. shows that increasing of annealing temperature to 700 °C and 750 °C leads to the continuous decrease of lattice parameter in the direction *c* in comparison with lattice parameters after annealing at the temperatures of 650 °C. This contraction indicates the incorporation of sodium ions in to the lattice, because additional positively charged Na^+ ions reduce the electrostatic repulsion between negatively charged cobalt oxides layers [65]. An exception from this trend is only observed for the NCO_1.0 sample at 750°C, for which the lattice parameter *c* increased compared to 700°C. The increase of lattice parameter *c* for NCO_1.0 can be explained by lack of sodium. This leakage is caused by the formation of sodium carbonate and was also observed for NCO_0.9/750 and for NCO_0.8/750. As it was noted in the previous section, the highest relative decrease of sodium due to carbonate formation is found for NCO_1.0/750. The parameter *c* is decreasing with increasing Na content in the case of the samples annealed at 650°C and 700°C (except for the reversed trend for $x = 0.8$ and 0.9), but for the samples heated at 750°C the parameters *c* tends to similar value for all *x*.

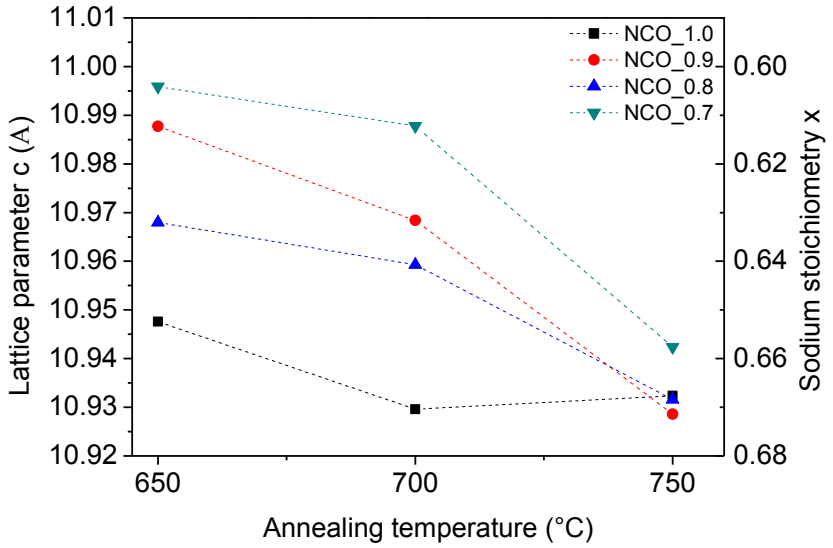

Figure 17. The dependence of lattice parameter *c* and the corresponding sodium stoichiometry *x* on the annealing temperature

We showed that the soft chemistry method is suitable for the preparation of sodium cobaltate phases. The crystallization of rhombohedral sodium cobaltate started during calcination at the temperature of 550 °C and we obtained pure rhombohedral phase by the annealing at the temperature of 600 °C. The hexagonal phase started to crystalize at the temperature of 650 °C and pure hexagonal phase without the rhombohedral phase can be obtained by the annealing at 750 °C. The use of soft chemistry method did not bring advantage in the lowering of the annealing temperature in comparison with the classical ceramic method reported in the work of *Y. Lei et al.* where the solid state reaction between spinel Co_3O_4 and Na_2O_2 was employed. Co_3O_4 and Na_2CO_3 phases are quite often observed as impurities in the synthesis of layered cobaltate [39] [51]. We showed that the phase composition of samples strongly depends on the initial sodium content and on the annealing temperature. Our results show that the sodium stoichiometry in hexagonal phase Na_xCoO_2 is independent on sodium precursor weight and the samples heat treated at 750 °C crystalized preferably with sodium stoichiometry around $x = 0.65$ (determined from lattice parameter *c*). The presence of spinel phase in diffraction patterns after calcination and the diffraction maxima of Na_2CO_3 after annealing at 750 °C suggests that sodium cobaltate phase is not formed directly from precursor gel. Probably, first the nanocrystalline spinel (Co_3O_4) particles formation takes place and that the reaction continues by classical solid state synthesis where the

spinel reacts with sodium cations into sodium cobaltate by diffusion flow. The temperature of decomposition of $Co(NO_3)_2.6H_2O$ and cobalt citrate followed by the formation of Co_3O_4 is below 450 °C [64] but this temperature is not sufficient for the formation of the pure rhombohedral phase Na_xCoO_2 because this formation is very slow even at the temperature of 550 °C. For this reason, we can still observe the presence of spinel up to the temperature of 600 °C. Despite of the formation of intermediated spinel phase, the soft chemistry method consisting in mixing of precursor on molecular scale represent progress in the comparison with classical ceramic method. The sol-gel method leads to the formation of spinel nanocrystallites of the size smaller than 50 nm (determined from integral breadth by Scherrer's equation) those represent very reactive solid state reactants, while classical ceramic method deals with the particles greater than 30 μm and the complete inter-diffusion requires much more time.

As sodium precursor, Na_2CO_3 is often use as it was published in many papers [41] [42] [43]. Also in our systems, we can observed the presence of Na_2CO_3 in the samples with higher sodium content in initial reactants. Once again, this carbonate is in nanocrystalline state and very reactive so it can participate in the cobaltate formation. Higher annealing temperature is favorable for incorporation of sodium into the cobaltate structure but on the other hand, the higher annealing temperatures lead to sodium volatility as it was reported e.g. by *Plewa et al*. [67]. They quantified the volatility of sodium from cobaltate during annealing by AAS. The sodium content decrease from 14.4 % ($Na_{0.66}CoO_2$) to 10.2 % ($Na_{0.45}CoO_2$) after 324 hours of annealing at the temperature of 900 °C. This fact limits the employed annealing temperatures to the value of 900 °C.

6.2.Elementary quantitative analysis

PXRD can determine only the amount of sodium, which is incorporated in the crystal structure. The use of AAS allows us to carry out the determination of the ratio between sodium and cobalt in a whole sample. The series of samples NCO_x/750 were analyzed also by AAS. The results are summarized in Table 6 where the results of PXRD analysis are also included for comparison. The phase composition and ratio between sodium and cobalt in the cobaltate structure [subcolumn Na:Co (Na:Co)] and the overall Na:Co ratio in the crystalline phases (subcolumn overall Na:Co) determined by PXRD are included in the PXRD column. The overall Na:Co ratio in the crystalline phases was determined by the following way: overall Na amount is the sum Na in cobaltate and Na in carbonate (determined from PXRD Rietveld analysis), overall Co amount is

the sum on Co in cobaltate and Co in spinel structure (also determined from PXRD Rietveld analysis).

Table 6. Na:Co ratio determined by AAS analysis for samples NCO_x/750 compared with quantitative PXRD analysis. The amount of Co_3O_4 and Na_2CO_3 in balance part is calculated from the proportions between Na:Co ratio obtained by the AAS and PXRD.

Analysis	AAS	PXRD					Minority phases balance	
Sample	Na:Co	Na:Co (NCO)	Phase composition [mol %]			Overall Na:Co	phase comp. [mol %]	
			Na_xCoO_2	Co_3O_4	Na_2CO_3		Co_3O_4	Na_2CO_3
NCO_0.7/750	0.60 ± 0.04	0.65	93.9	6.1	-	0.55	2.7	-
NCO_0.8/750	0.70 ± 0.04	0.66	89.8	-	10.2	0.80	-	2.0
NCO_0.9/750	0.73 ± 0.05	0.67	80.7	-	19.3	0.93	-	2.9
NCO_1.0/750	0.79 ± 0.05	0.66	77.3	-	22.7	0.96	-	6.1

The AAS analysis showed that after final annealing at 750°C, the content of sodium in real samples is lower than it is in the nominal composition of precursor. The sodium losses are in the range from 14 mol % for the NCO _0.7/750 to 21 mol % for the NCO_1.0/750. The decrease of sodium content is quite high in comparison with the literature [68] [69]. The 10 mol % excess of sodium precursor is commonly used for preparation. These high losses in our case could be due to longer calcination time (72 hours) and annealing (480 hours for sample annealed at 750 °C). *Motohashi et al.* studied reaction between Na_2CO_3 and Co_3O_4 by the TG analysis. The reported weight loss between 500 and 750 °C was of 7.5 %, which is quite high and only 5.7 % can be explained by CO_2 losses. They assumed that the rest of observed weight loss (1.8 %) is due to Na evaporation below 600 °C where the chemical reaction is slow yet [68] and they propose to anneal the samples directly at 750 °C in order to suppress the sodium volatility. The proper heat treatment at low temperature is required in our case because we need to remove the organic part from precursor and to eliminate the residual carbon content [58].

The sodium balance was determined by the following way: by the value of Na:Co in sodium cobaltate phase determined by PXRD [column PXRD subcolumn Na:Co (NCO)] was subtracted from : the value of ratio Na:Co determined by AAS (column AAS Na:Co). Negative resulting value corresponds to the deficiency of sodium and presence of Co_3O_4. Positive resulting value corresponds to the excess of Na in the form of Na_2CO_3. The molar values of minority phases

(Na_2CO_3 and Co_3O_4) were calculated then from these resulting value (*Z*) (column "Minority phases balance phase comp. [mol %]").

We can see from Table 6 that the molar amount of Na_2CO_3 (about 20 mol %) determined using PXRD is unrealistically high and is not coherent with AAS results. We provided following minority phase determination analysis, which combines result from both AAS and PXRD due to general lower accuracy of standardless quantitative PXRD methods based on Rietveld refinement. The mol % of Na_2CO_3 and Co_3O_4 calculated from sodium balance shows that the amounts of minority phases determined by PXRD analysis are overestimated.

The conclusion from these quantitative elementary analysis shows that the sodium content in nominal composition of reaction differ from overall sodium content in final samples due to volatility of sodium. We also determined that the amount of sodium in cobaltate structure is different due to presence of minority phases.

6.3.Seebeck coefficient of α- and γ- phase

This chapter deals with the dependence of Seebeck coefficient on sodium stoichiometry and the evolution of thermopower for hexagonal γ- phase and rhombohedral α- phase. The summary of Seebeck coefficient measurements is presented here. Two series of samples NCO_x/600 (rhombohedral α-phase) and NCO_x/750 (hexagonal γ-phase) were chosen for these measurements.

Figure 18 shows the dependences for Seebeck coefficient on temperature for the series of NCO_x/600 samples. We know from PXRD analysis that after annealing at 600 °C, the samples form rhombohedral α-phase of Na_xCoO_2. Co_3O_4 spinel is present as minority phase in samples heated at 600°C and in NCO_0.7/750 (as deduced from susceptibility data), but always in such small amount that has no significant influence on Seebeck coefficient.

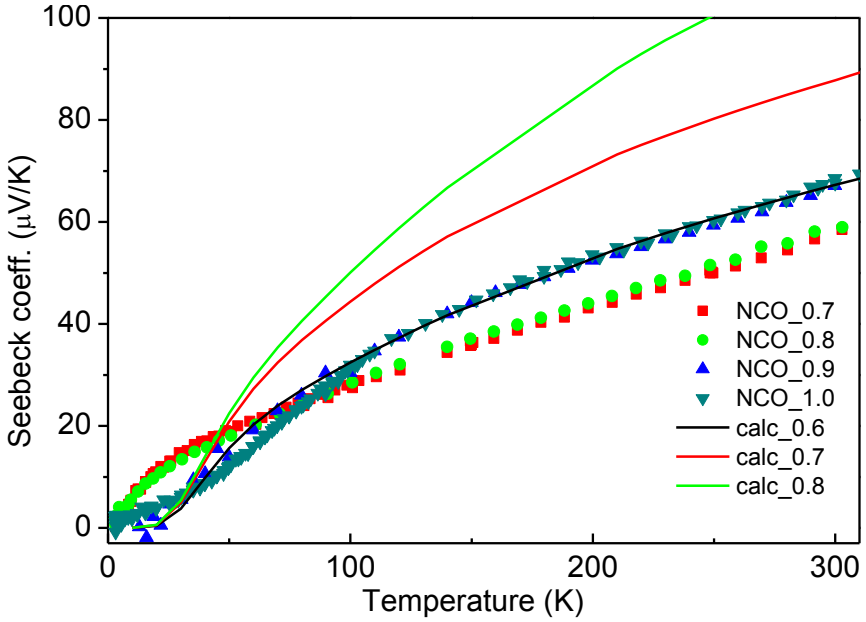

Figure 18. Dependence of thermopower *S* on temperature for rhombohedral phase Na_xCoO_2. The calculated dependence is presented by solid curves.

For the rhombohedral phases, we can identified two behavior of the Seebeck coefficient on temperature (fig. 18). The samples NCO_0.7/600 and NCO_0.8/600 exhibit similar temperature dependence with sharp slope below 25 K and then the increase is slower. For the samples NCO_0.9/600 and NCO_1.0/600, slow rise under 20 K is typical. Between 25 K and 125 K, Seebeck coefficient rapidly grows and at ~75 K, it shows higher value in comparison with the samples with lower sodium stoichiometry. The solid lines in Figure 18 present the theoretical dependences of Seebeck coefficient for rhombohedral phase calculated by DFT.

Seebeck coefficients for the samples heat treated at 750 °C plotted in Figure 19 exhibit similar values in the temperature range of 100 to 300 K. Two type of behaviors of the thermopower *S* were observed like in NCO_x/600 samples. Seebeck coefficient for samples NCO_0.7/750, NCO_0.8/750 and NCO_0.9/750 exhibits negative values below 10 K and it is close to zero between 10 and 20 K.

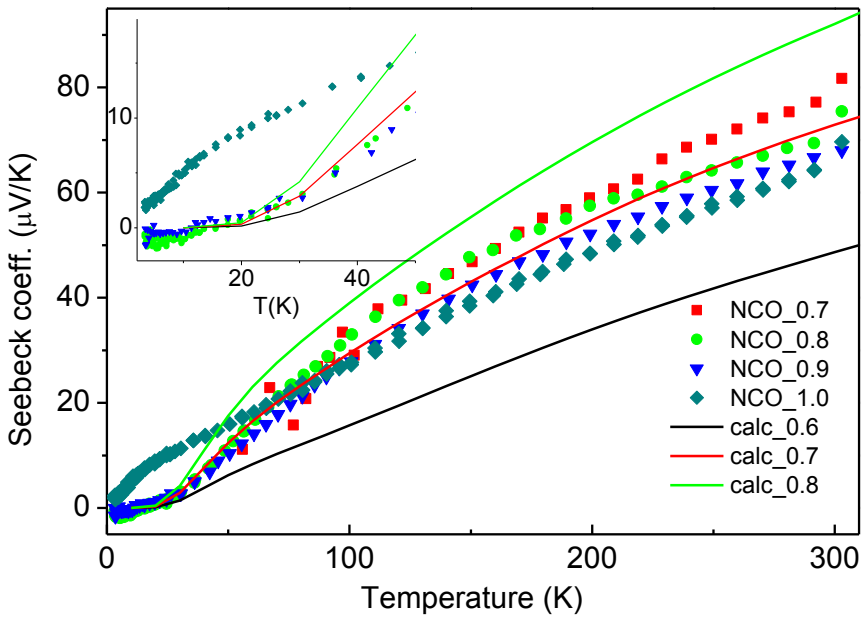

Figure 19. Dependence of thermopower *S* on temperature for hexagonal phase Na_xCoO_2. The solid curves present the calculated dependence of Seebeck coefficient *S*. The inset provide detailed look on Seebeck coefficient below 50 K.

The experimental data of sodium rich samples NCO_1.0/600 and NCO_0.9/600 fit to theoretical calculation for sodium stoichiometry $x = 0.6$. So we can hypothesize that real sodium stoichiometry in these samples is $x = 0.6$. The experimental values for the samples NCO_0.8/600 and NCO_0.7/600 lies below the calculated curve for $x = 0.6$. So in this case, the real Na stoichiometry is probably below $x = 0.6$. Rhombohedral phase is less studied in comparison with hexagonal phase and for this reason, we couldn´t compared our experimental and calculated data with literature.

Seebeck coefficient for the series of samples NCO_x/750 does not show systematic evolution in comparison with the rhombohedral phase (NCO_x/600). With increasing sodium stoichiometry, we do not observe the increase of the thermopower. Probably, the real Na stoichiometry after heat treatment at 750 °C for all samples is close to the $x = 0.7$ as follow from the comparison with theoretical calculation. This invariance of x on initial composition is in agreement with PXRD measurement where the same tendency of Na stoichiometry was found. Higher values of Seebeck coefficient for hexagonal phases (NCO_x/750) (corresponding to $x = 0.7$) in comparison with rhombohedral phase (NCO_x/600) (corresponding to $x = 0.6$) is in good agreement with the fact that at higher temperature, more sodium atoms enter cobaltate structure. It seems that it would be suitable to heat treated the samples at higher temperature than

750 °C in order to incorporate higher amount of sodium into the cobaltate structure. Nevertheless, this process has its limitation in the fact that higher temperature leads to the higher loss of sodium due to thermal evaporation.

Two behaviors of Seebeck coefficient at low temperature indicates the presence of both positive and negative carriers, because the thermopower *S* is sensitive to a change in topology of a Fermi surface [69] *Y. Okamoto et al*. observed similar behaviors of the thermopower at low temperatures on the samples with sodium stoichiometry $x = 0.55$, 0.61, 0.63 and 0.72. We observed the similar dependence of sodium stoichiometry for the sample NCO_1.0/750 as *Okamoto* found for of $x = 0.55$ and 0.61 with the positive values of *S*. Their interpretation is that a Fermi surface consists of single hole sheet. Below 50 K, in the case of the samples with $x = 0.63$ and 0.72, the Seebeck coefficient is almost zero ($x = 0.63$) or reaches the negative values ($x = 0.72$). These results indicate that the both positive and negative carriers exist for $x > x^*$ (critical value of sodium stoichiometry), where x^* is found in very narrow range of $0.620 < x^* < 0.621$.

In the published papers, the thermoelectric properties of layered cobaltate Na_xCoO_2 are studied at the temperatures higher than room temperature up to 700 K due to potential application of γ- phase as high temperature thermoelectric material, but few papers are devoted to low temperature studies of thermopower [32] [33] [68] [69]. They showed that Seebeck coefficient measured at 300 K lies in the range from 55 μV/K for $x = 0.55$ to 75 and 120 μV/K for $x = 0.65$ and 0.75. Seebeck coefficient measured on our samples is in the range from 70 to 80 μV/K. From the comparison with published results, we can conclude that sodium stoichiometry of our γ- phase is between 0.65 and 0.75.

The resistivity and thermal conductivity measurements were done for selected samples in order to complete the study of transport properties. The resistivity measurements for samples annealed at the temperature of 750°C are shown in figure 20. The experimental data clearly show that prepared samples exhibit metallic type conductivity with resistivity values within the range ~0.5 – 1 mOhm·cm at 3 K and from ~4 to ~6 mOhm·cm at 300 K

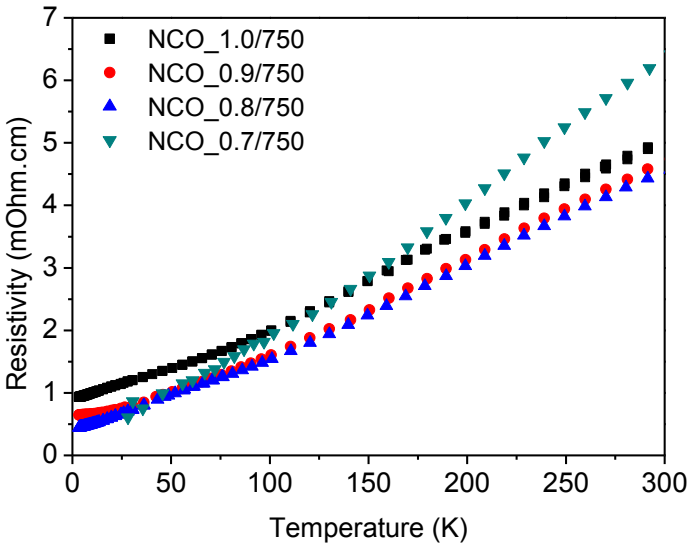

Figure 20. Temperature dependence of resistivity for the serie of samples annealed at the temperature of 750 °C.

The thermal conductivity measurements (after correction on radiation) for the samples annealed at the temperature of 750°C are shown in figure 21. The values of thermal conductivity are between 2 – 3 $WK^{-1}m^{-1}$ at 300 K, which are typical values for Na_xCoO_2. [70]. The typical enhancement of thermal conductivity at low temperatures, which is related to the gradual prolongation of the mean free path of phonons with decreasing temperature, is reduced or even suppressed (x = 0.8) due to the static disorder introduced by Na vacancies.

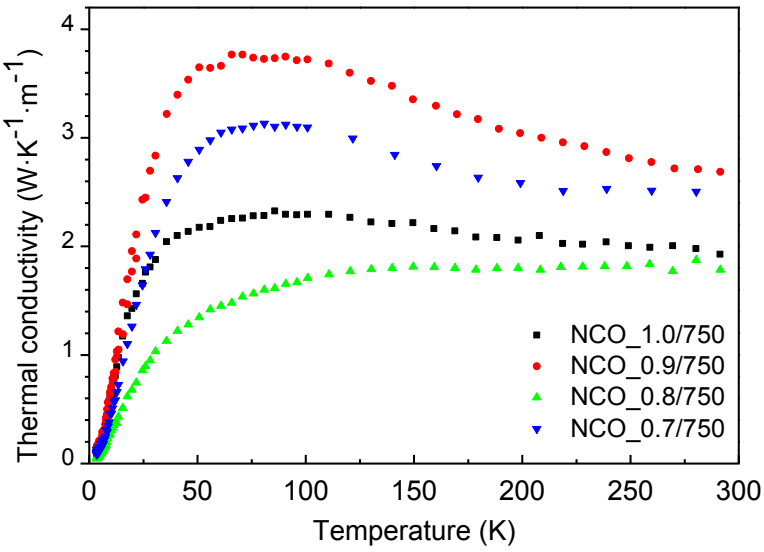

Figure 21. Dependence of thermal conductivity on temperature for the series of samples annealed at the temperature of 750 °C.

6.4.Magnetic susceptibility

The FC and ZFC temperature dependence of magnetic susceptibility were carried out under magnetic field 1 T or 0.1 T for samples annealed at the temperature of 600 °C and 750 °C. Since Na^+ is nonmagnetic, the Curie-Weiss behavior of $\chi(T)$ is attributed to the distinct Co^{3+} and Co^{4+} ions arranged at the cobalt ion sites [71]. The magnetic susceptibilities were analyzed by modified Curie-Weiss law:

$$\chi_i = \chi_i^0 + \frac{C_i}{T - \theta_i}$$

where χ_i^0 represents the temperature-independent contributions, which include the van Vleck paramagnetism, diamagnetism of core electrons Landau diamagnetism of itinerant electrons and the Pauli susceptibility, C_i is Curie temperature and θ_i represents the Weiss constant [72] [73].

The analysis was performed in several steps. The paramagnetic contribution from spinel and the temperature independent contributions were subtracted from measured susceptibility firstly. The magnetization measurement is very sensitive to the presence of Co_3O_4 and CoO, which are antiferromagnets with T_N =35 and 292 K, respectively [71]. The presence of Co_3O_4 in our samples was manifested by the "hump" observed in reciprocal susceptibilities at 30 K. The Co_3O_4 contents were determined by simple subtraction of antiferromagnetic Co_3O_4 contribution.

After that the data of reciprocal susceptibility $1/\chi$ was fitted by linear regression and Weiss and Curie constant were deduced and the effective magnetic moment was then calculated. The Curie temperature is determined from the slope of linear regression of $1/\chi$ because value $1/C_i$ is equal to the slope and Weiss constant as the intersection with $1/\chi$ axis divided by C_i. The effective magnetic moment was than calculated by the formula:

$$\mu_{\text{eff}} = \sqrt{\frac{3 \cdot C \cdot k_{\text{B}}}{N_{\text{A}} \cdot \mu_B^2}}$$

Which was used for determination of spin value S from equation:

$$\mu_{\text{eff}} = g \cdot \sqrt{S \cdot (S+1)}$$

The tabulated values were chosen for van Vleck and diamagnetic contribution of core electrons. In order to calculate the contribution of the Pauli susceptibility to the constant term, we have to know the value of electron effective mass m^*:

$$\chi_{Pauli} = \frac{\chi_{const} - \chi_{vV} - \chi_{dia}}{1 - \frac{1}{3(m^*)^2}}$$

The value of effective mass can be estimated by comparison with specific heat, namely using the Wilson ratio between Sommerfeld coefficient γ and Pauli susceptibility $\gamma/\chi_P = 72.91$ [74]. The agreement with the experimental γ, which was measured within the range 18-20 $\text{mJ}\cdot\text{K}^{-2}\cdot\text{mol}^{-1}$ for selected samples, was obtained for $m^* = 2$.

Figure 22 showed the ZFC dependence of magnetic susceptibility and the reciprocal magnetic susceptibility $1/\chi$ for sample annealed at the temperature of 750°C. The reciprocal susceptibility $1/\chi$ data between 100 K and 350 K was fitted by the linear regression. The results are summarized in Table 7.

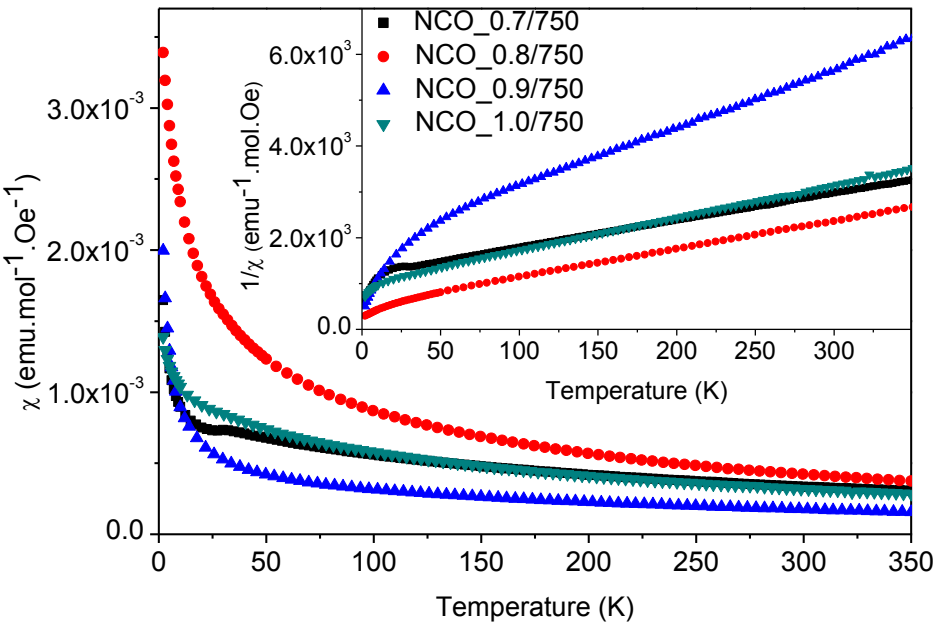

Figure 22. The susceptibility and reciprocal susceptibility after subtraction of linear contributions for the samples annealed at 750 °C.

Table 7. The results of susceptibility analysis for samples NCO_x/750. The average values are written by bold font.

Sample		χ_{dia}	χ *van Vleck*	χ *Landau*	χ *Pauli*	χ *const.*	$\mu^2_{eff.}$ [μ_B]	*S*	Θ [K]
NCO_	ZFC 1 T	-37	70.25	-21.07	252.84	265	1.35	0.27	-202.91
0.7/750	FC 0.1 T	-37	70.25	-17.43	209.20	225	1.73	0.33	-249.04
	ZFC 0.1 T	-37	70.25	-24.25	291.02	300	1.19	0.24	-183.82
						263.33		**0.28**	**-211.92**
NCO_	ZFC 1 T	-37.5	70.25	-18.39	220.65	235	1.31	0.26	-89.203
0.8/750	FC 0.1 T	-37.5	70.25	-18.39	220.65	235	1.19	0.24	-72.463
	ZFC 0.1 T	-37.5	70.25	-18.39	220.65	235	1.19	0.24	-78.72
						235.0		**0.25**	**-80.13**
NCO_	ZFC 1 T	-37.7	70.25	-22.49	269.9	280	0.63	0.14	-149.21
0.9/750	FC 0.1 T	-37.7	70.25	-22.49	269.9	280	0.63	0.14	-131.9
	ZFC 0.1 T	-37.7	70.25	-22.49	269.9	280	0.64	0.14	-137.89
						280.0		**0.14**	**-139.67**
NCO_	ZFC 1 T	-37.9	70.25	-22.06	264.75	275	1.13	0.23	-143.86
1.0/750	FC 0.1 T	-37.9	70.25	-20.70	248.38	260	1.25	0.25	-155.88
	ZFC 0.1 T	-37.9	70.25	-18.88	226.57	240	1.37	0.27	-171.39
						258.33		**0.25**	**-157.04**

The sample NCO_0.7/750 contains 6.1 mol % of spinel, as it was determined by the PXRD. The content of Co_3O_4 spinel 2.0 mol % was determined by simple subtraction of antiferromagnetic

contribution of Co_3O_4 from global susceptibility. The difference between amount of spinel determined by PXRD (6.1 mol %) and χ measurement for sample NCO_0.7/750 is rather high, and probably the determination is loaded due to inaccuracy which was discussed in the previous chapter.

The subtraction of the temperature independent contribution (the sum of van Vleck, core electrons, Landau and Pauli contributions) to the global magnetic susceptibility linearizes the $1/\chi$ in temperature range from 100 to 350 K. The constant contribution for samples NCO_x/750 is between ~235.10^{-6} (NCO_0.8/750) and 280.10^{-6} $emu.mol^{-1}Oe^{-1}$ (NCO_0.9/750), which are values comparable with literature [71] [75].

The determined Weiss temperature for series of γ- Na_xCoO_2 samples is always negative in sign as we expected for antiferromagnetic spin interactions [68] and it increases from −212 K for sample NCO_0.7/750 to −80 K (NCO_0.8/750). Nevertheless, we do not observed gradually incensement of the Weiss temperature and spin with rising sodium stoichiometry as was expected [36] [75].

The ZFC susceptibility χ and $1/\chi$ for series of samples NCO_x/600 are shown in Figure 23 and the results of analysis are summarized in Table 8. The amount of spinel was determined by the same way as for the hexagonal phase and is summarized in Table 8. The temperature independent contribution χ_{const} wasn´t considerer in the case of rhombohedral samples (NCO_x/600) due to negative fitted values of χ_{const}, which are incorrect from the physical point of view. The reciprocal susceptibility $1/\chi$ was fitted in temperature range from 250 to 350 K.

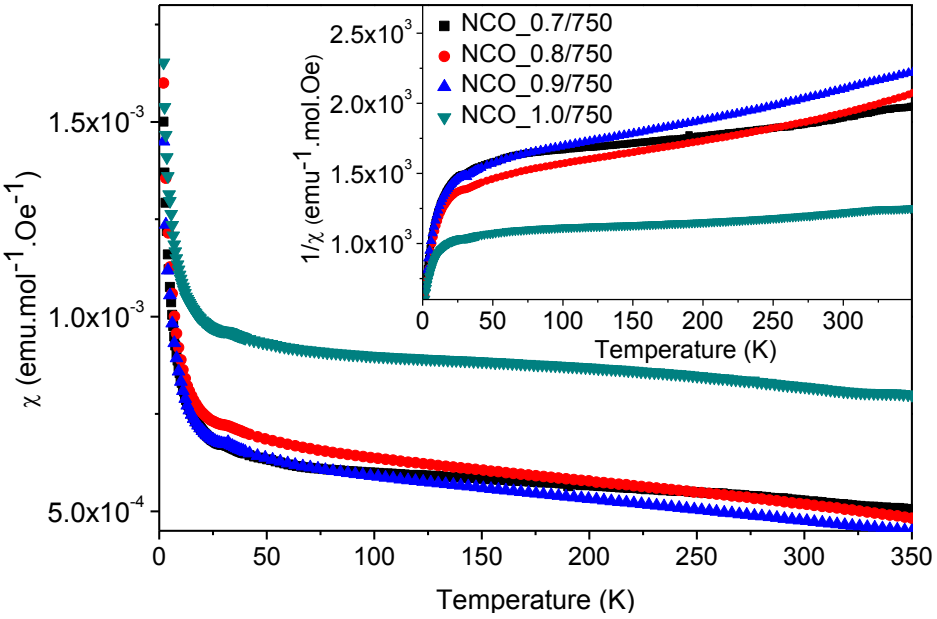

Figure 23. The susceptibility and reciprocal susceptibility after subtraction of linear contributions for the series of samples annealed at 600 °C (NCO_x/600).

Table 8. The results of susceptibility analysis for samples NCO_x/750. The average values are written by bold font.

Sample		Co_3O_4 [mol %]	$\mu^2_{eff.}$ [μ_B]	S	Θ [K]
NCO_ 0.7/600	ZFC 1 T	2.5	4.80	0.70	-839.24
	FC 1 T		4.31	0.65	-783.75
				0.68	**-811.49**
NCO_ 0.8/600	ZFC 1 T	-	3.21	0.53	-476.88
	FC 1 T		3.25	0.53	-482.89
				0.53	**-479.88**
NCO_ 0.9/600	ZFC 1 T	1.0	3.28	0.53	-562.42
	FC 1 T		3.20	0.53	-542.06
				0.53	**-552.24**
NCO_ 1.0/600	ZFC 1 T	1.0	10.45	1.19	-1291.46
	FC 1 T		9.58	1.13	-1146.48
				1.16	**-1218.97**

In the case of rhombohedral series of samples (NCO_x/600), the presence of Co_3O_4 spinel is in range from 1 to 2.5 mol % in the rhombohedral samples NCO_0.7/600, NCO_0.9/600 and NCO_1.0/600. The obtained paramagnetic temperatures are very high in comparison with those, which we obtained for similar hexagonal phase. The same was also found for S values. The $1/\chi$ after subtraction of the spinel contribution manifests the broad wave on the curves between 50 and 250 K. For this reason, only data above 250 K where the curves exhibit linear behaviors were used

for the linear regression. The presence of these waves could explain why our analysis provide slightly different values in comparison with hexagonal phase.

The broad hump at 50 - 200 K on reciprocal susceptibility curves has no physical meaning. It can be due to incorrect Co_3O_4 data for subtraction, which were taken from bulk standard Co_3O_4 sample, which represent different particle morphology.

For better correction (subtraction of spinel susceptibility contribution), the Co_3O_4 was prepared by the same way as Na_xCoO_2 in order to assure similar sample morphology. This Co_3O_4 was then measured at the same condition and resulting data were used for subtraction of spinel contribution. The corrected data of susceptibility for α- Na_xCoO_2 treated by this way fitted better with expected linear behavior and the hump was not so significant.

The magnetism in Na_xCoO_2 is related to the Na vacancies ($x < 1$). A single Na vacancy creates a hole in Co-t_{2g} orbital, change its occupation from t_{2g}^6 to t_{2g}^5 and induces an S = 1/2 local moment. With increasing doping the holes may become itinerant, which is manifested by metallic type resistivity and occurrence of itinerant magnetism. The Na vacancies are mostly randomly ordered and their distribution is not perfectly uniform. The holes in the regions with enhanced electrostatic potential fluctuations due to the disordered Na vacancies are more localized, whereas the regions with less potential fluctuations allow itinerant behavior of the holes. Thus, the magnetic properties of Na_xCoO_2 are characterized by the coexistence of localized and itinerant electronic states and the simple relation between hole doping (1-x) and magnetic moment, valid for localized magnetic moments, is not preserved [76].

6.5.Oriented Na_xCoO_2 thin films

The series of thin films deposited on α-Al_2O_3 (00l) single crystal substrates were prepared by CSD technique. Samples were characterized by PXRD using standard $\theta - \theta$ scans and ω scans. For some selected samples, the measurement of φ scans were carried out. In Figures 24-27, we can follow the $\theta - \theta$ scans measured on four series of samples prepared from coating solutions with different initial Na content (fig. 24 x =1.0, fig. 25 x = 0.52, fig. 27 x = 0.35, and fig. 27 x = 0.175) heat-treated at the temperatures of 750, 800, 850, and 900 °C. One set of patterns corresponds to the samples of the same precursor sol (the same Na content). The results of phase composition analysis are summarized in Table 9.

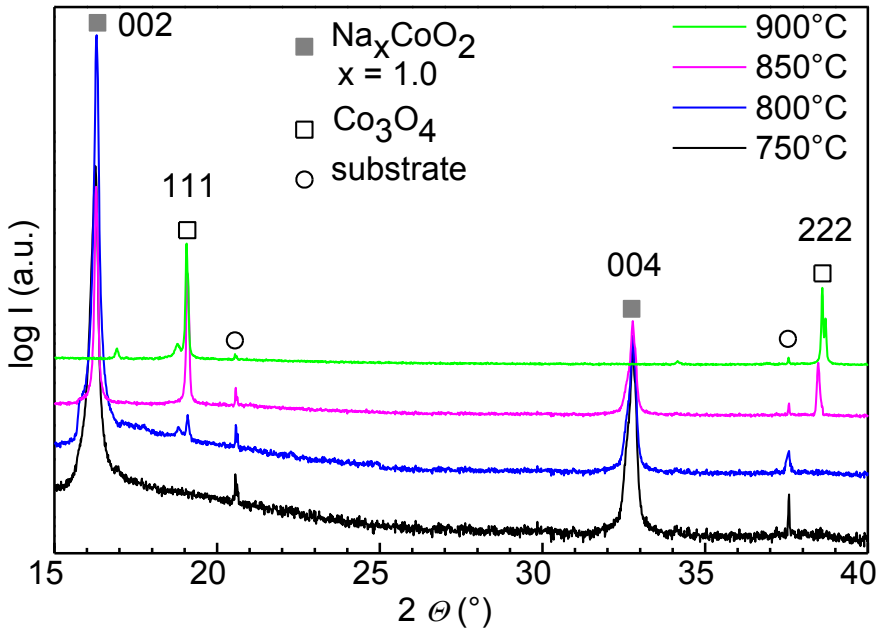

Figure 24. The θ − θ patterns of thin films prepared using the coating solutions with initial sodium stoichiometry x = 1.0.

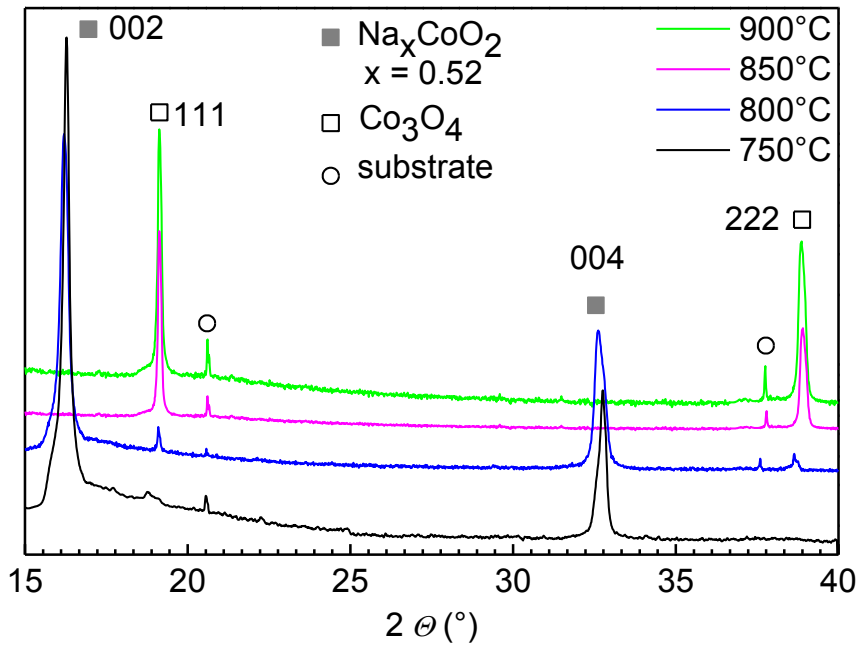

Figure 25. The $\theta - \theta$ patterns of thin films prepared using the coating solutions with initial sodium stoichiometry x = 0.52.

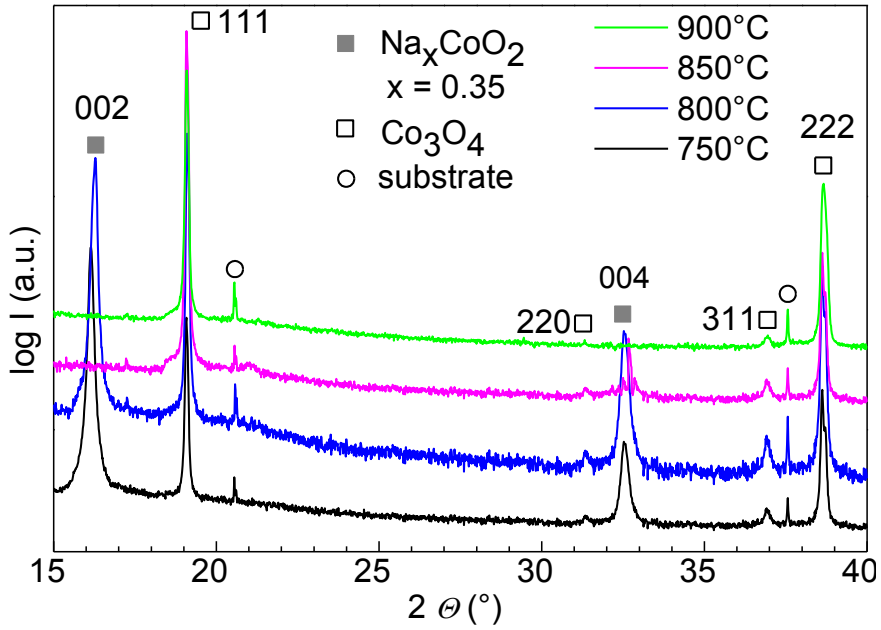

Figure 26. The $\theta - \theta$ patterns of thin films prepared using the coating solutions with initial sodium stoichiometry x = 0.35.

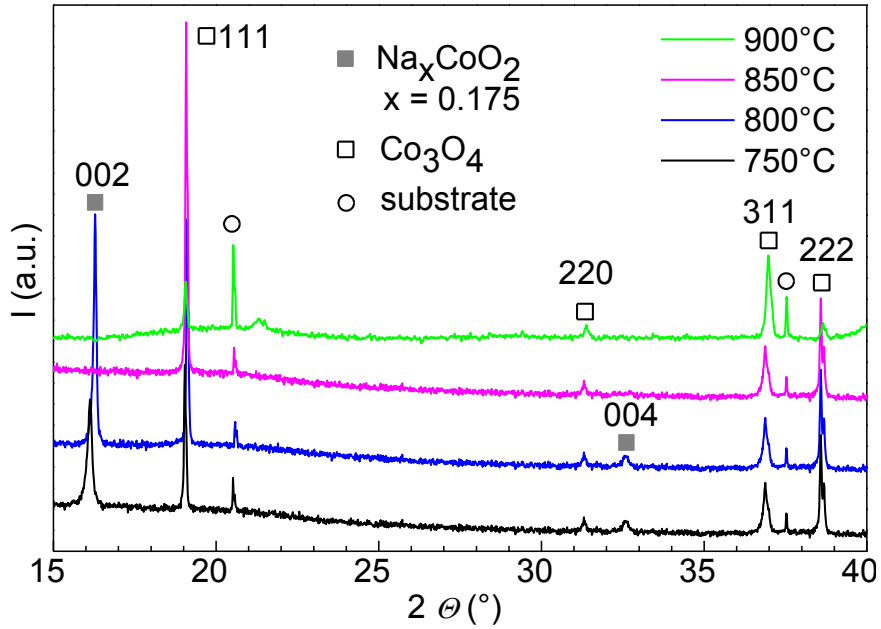

Figure 27. The $\theta - \theta$ patterns of thin films prepared using the coating solutions with initial sodium stoichiometry x = 0.175.

The XRD patterns of series of thin films with initial sodium stoichiometry x = 1.0 are showed in Figure 24. Only diffractions maxima of Na_xCoO_2 phase are observed for the sample annealed at 750 °C. The use of higher annealing temperatures above 750 °C leads to crystallization of Co_3O_4. The thin films annealed at 800, and 850 °C are formed by both Na_xCoO_2 and Co_3O_4 phases. After the annealing at 900 °C, only Co_3O_4 diffraction maxima were observed. Sodium cobaltate Na_xCoO_2 and Co_3O_4 exhibit preferential orientation because only diffraction maxima corresponding to the planes with Miller indexes *hkl*, where $h = k = 0$ for Na_xCoO_2 phase and $h = k = l$ for Co_3O_4 were observed.

The thin films prepared by deposition of coating solution with initial sodium stoichiometry x = 0.52 (Figure 25) exhibit similar dependence of phase composition on annealing temperature as for series with x = 1.0. The difference is that diffraction maxima of spinel phase for sample annealed at 800 °C are more intensive and that the pure spinel film was obtained at the temperature 850 °C for samples with x = 0.52.

The films with initial sodium stoichiometry x = 0.35 and 0.175 (Figure 26 and Figure 27) contain spinel even after annealing at 750 °C and Na_xCoO_2 was observed only in the samples annealed at 750 and 800 °C. In comparison with diffraction patterns of the series with x = 1.0 and

0.52, the diffraction maxima of spinel phase assigned to *hkl* reflection with $h \neq k \neq l$ were observed that indicates crystallization of randomly oriented spinel phase.

The diffraction pattern of film prepared by deposition of Co_xO_y coating solution ($x = 0$) (Figure 28) shows randomly oriented Co_3O_4 after annealing at 900 °C. This film was prepared for the demonstration of crucial role of Na_xCoO_2 on the oriented growth of Co_3O_4 on α-Al_2O_3.

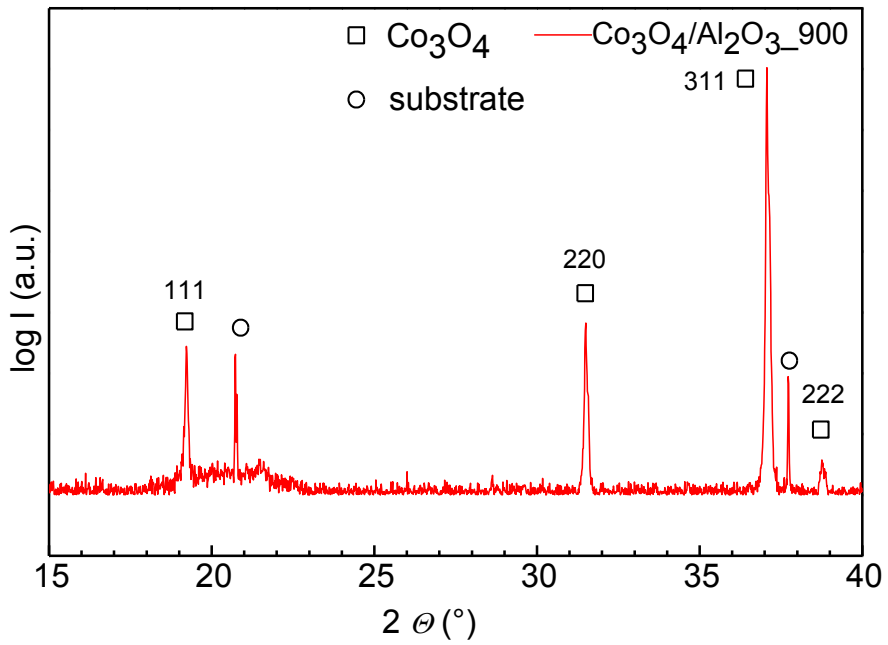

Figure 28. Co_3O_4 film prepared by deposition of Co_xO_y coating solution ($x = 0$) on α-Al_2O_3 after annealing at 900 °C

For semi-quantification of out of plane orientation, Ω scans were measured on 002 diffraction of Na_xCoO_2 sample and on diffraction 111 for Co_3O_4. Figure 29 shows XRD patterns of Ω scans measured on 111 diffraction of Co_3O_4 prepared from coating solutions with different initial sodium stoichiometry ($x = 1.0$, 0.52, 0.32, and 0.172) and heat treated at 900 °C. Other Ω scan measurements are not presented here in detail, the results of their measurements are only summarized in Table 9. Obtained Ω curves were fitted by Gauss function using Winplotr software (Fullprof package software). Although no exact physical justification exists for the use of Gauss function for fitting of omega curves, the global shape of Gauss function and the parameter of full width at half maxima (FWHM) and the area under curve helped us to quantify the out of plane

orientation. Two behaviors of Ω curves were occurred and we suggest that in our samples two orientation growths modes (bimodal distribution) took place. The narrow component presents the fraction of crystallites, which are oriented with a small deviation from parallel orientation to the substrate. The broad component (observed in bimodal distribution – see Fig. 29a and Fig. 29d) represents the crystallites for which the deviation is higher and the corresponding planes are not exactly parallel to the substrate.

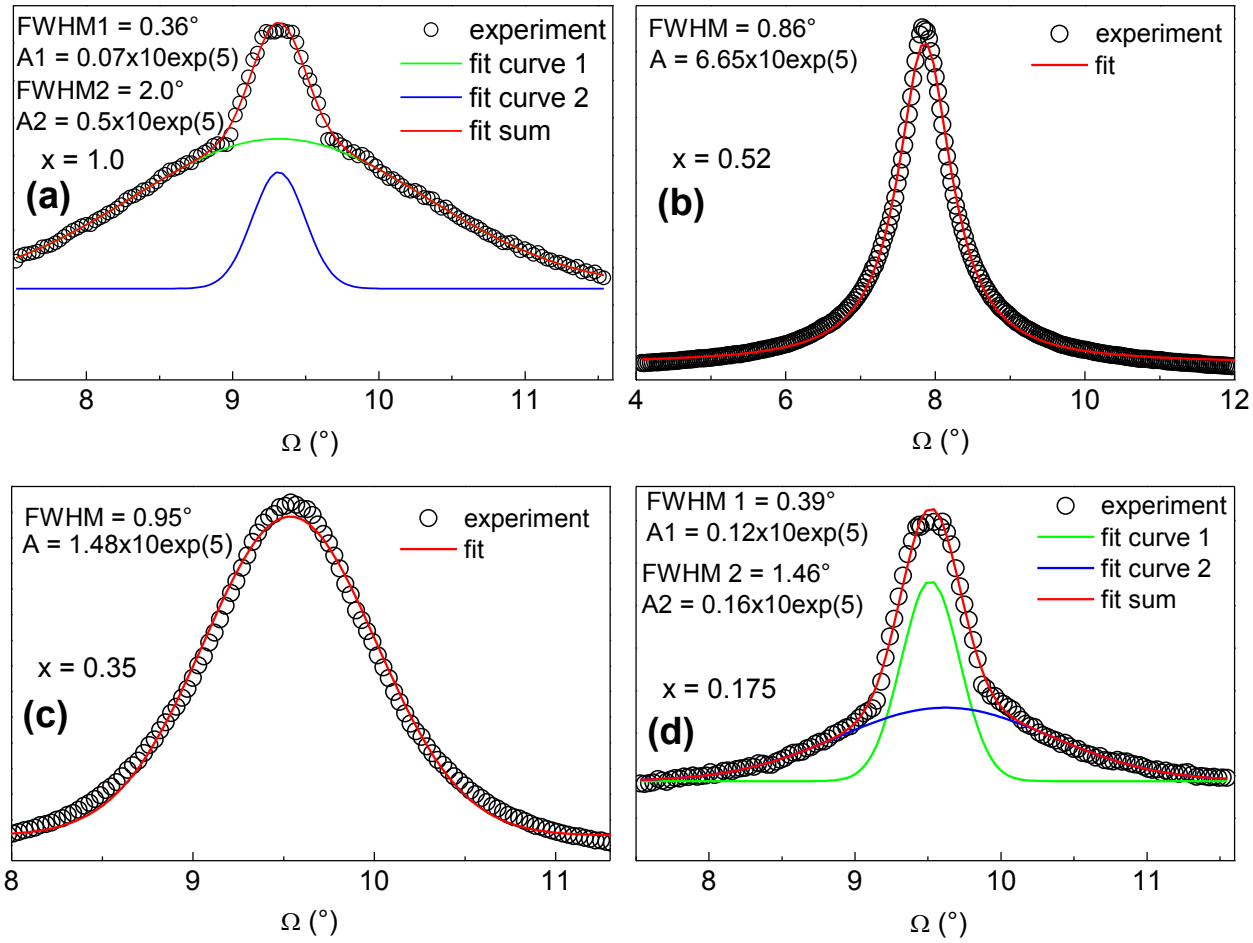

Figure 29. The XRD patterns of Ω scans measured on 111 spinel Co_3O_4 diffraction for thin film prepared from coating solution with different initial sodium stoichiometry (a) x= 1.0, (b) x =0.52 (c) x =0.35 and (d) x= 0.175 and annealed at the temperature of 900 °C.

The analysis of Ω curves showed that out-of-plane orientation of Na_xCoO_2 and Co_3O_4 is affected by the initial sodium stoichiometry x. The coating solution with x = 0.52 was chosen as the optimal coating solution for preparation of well oriented Co_3O_4 films. From these Ω curve measurements, it follows that using of coating solutions with higher or lower sodium content

decrease the volume of well oriented crystallites, which manifest higher values of FWHM or bimodal Ω curves. The bimodal shape was observed for Co_3O_4 prepared by decomposition of sodium cobaltate Na_xCoO_2 thin films prepared from the coating solution with initial sodium stoichiometry x = 1.0 and 0.175. We think that the bimodal shape of omega curve in the case of the most concentrated Na sample (x = 1.0) showed in Figure 29a is caused by massive sodium migration (diffusion or evaporation) from the whole volume of layer that leads to greater deterioration of the film quality during annealing. On the other hand, the bimodal shape of omega scan in the case of the least concentrated Na sample (x = 0.175 Figure 29d) can be due to the fact that the amount of sodium in the coating solution is below the region of sodium cobaltate stability ($x \geq 0.30$) and Na_xCoO_2 phase forms only part of thin film. The remaining cobalt precursor forms randomly oriented Co_3O_4 phase.

Table 9. The summarization of phase composition and FWHM values of Ω curves for samples prepared from coating solutions with different sodium stoichiometry (x = 0.175, 0.35, 0.52, 1.0) and heat-treated at the temperatures of 750, 800, 850 and 900 °C. The label (bm) indicates bimodal shape of omega curve, symbol D denotes decomposition of Na_xCoO_2 and N symbolizes no diffraction maxima corresponding to Co_3O_4.

x(Na_xCoO_2)	750 °C	800 °C	850 °C	900 °C	hkl used for ω scans
0.175	0.50° (bm)	D	D	D	002 (Na_xCoO_2)
	0.50°	0.60°	0.55° (bm)	0.60° (bm)	111 (Co_3O_4)
0.35	1.30°	1.40°	D	D	002 (Na_xCoO_2)
	0.80°	1.0°	1.1°	1.0°	111 (Co_3O_4)
0.52	0.80°	1.10°	D	D	002 (Na_xCoO_2)
	N	N/A	1.65°	0.90°	111 (Co_3O_4)
1.0	2.60° (bm)	3.20° (bm)	3.20° (bm)	D	002 (Na_xCoO_2)
	N	N/A	0.60° (bm)	0.40° (bm)	111 (Co_3O_4)

The standard $\theta - \theta$ and Ω scans provide information on the d spacing only along the direction perpendicular to the substrate surface. The sample showing the best texture (the most narrow single mode Ω curves) where the in-plane orientation was expected, were characterized by φ scan. The diffractions indexed as $10\bar{1}4$ (2θ = 35.14°, ψ = 38.24°) and $11\bar{2}3$ (2θ = 43.36°, ψ = 61.21°) in hexagonal notation for α-Al_2O_3 substrate were used for φ scan measurement. For Co_3O_4 film, we used the 400 (2θ = 44.88°, ψ = 54.70°) and 220 (2θ = 31.28°, ψ = 35.20°)

diffractions. The φ scan on 400 diffraction for Co_3O_4 thin film prepared from coating solution with x = 0.52 and annealed at 900 °C shows six maxima separated by 60° and aligned with $11\bar{2}3$ and $10\bar{1}4$ poles of substrate. The φ scan on 220 exhibit 12 maxima separated by 30° also aligned with $11\bar{2}3$ α-Al_2O_3 and $10\bar{1}4$ poles for α-Al_2O_3 substrate (fig. 30).

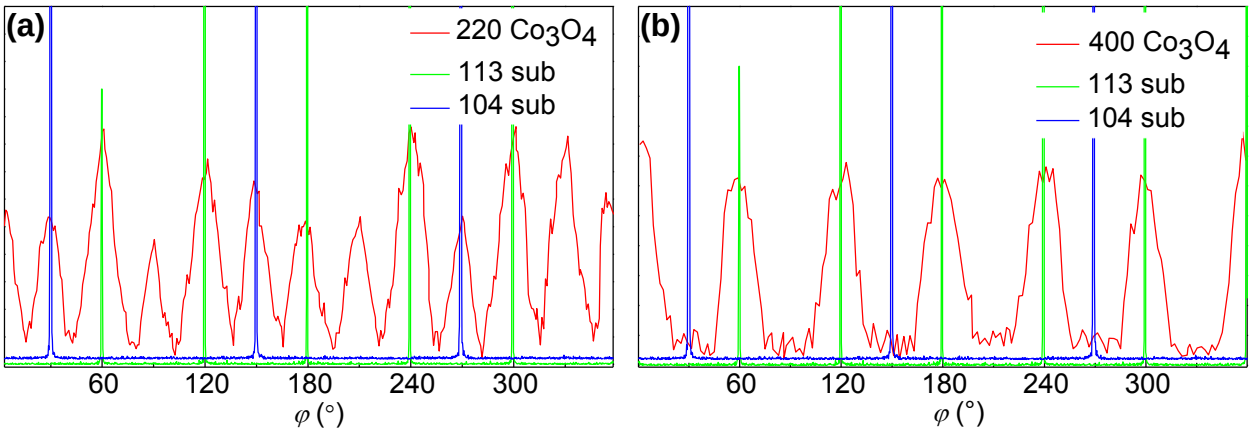

Figure 30. The scans of Co_3O_4 thin films measured on: (a) 220 and (b) 400 diffractions coupled with φ scans of α-Al_2O_3 substrate measured on 113 ($11\bar{2}3$ hexagonal notation) and 104 ($10\bar{1}4$ hexagonal notation) diffractions.

This six fold (diffraction 400) and twelve fold (diffraction 220) symmetry in φ scans observed for spinel structure and their coincidence with the substrate maxima prove unique in-plane orientation relation between the film and the substrate. The multiplicity of planes 400 and 220 are 6 or 12, respectively. The φ scans were measured only for one hemisphere of whole pole sphere. In an ideal case, for planes 400, we should observe three diffraction maxima separated by 120° while for planes 220, six maxima separated by 60° should be observed. Therefore, measured φ scans indicate occurrence of two types of growth modes in our samples, which have the same out of plane orientation [111] with ⟨011⟩ and ⟨110⟩ planes rotated by 180° into mirror direction. These in-plane twins are formed during the ordering of the O^{2-} layers (A-B-C-A… and A-C-B-A…) in cubic close packing (Figure 31). The average FWHM values of φ scans for Co_3O_4 film are larger than respective scans for substrate, or scan published for Co_3O_4 films prepared by more sophisticated deposition (e.g. PVD) methods [77] [78].

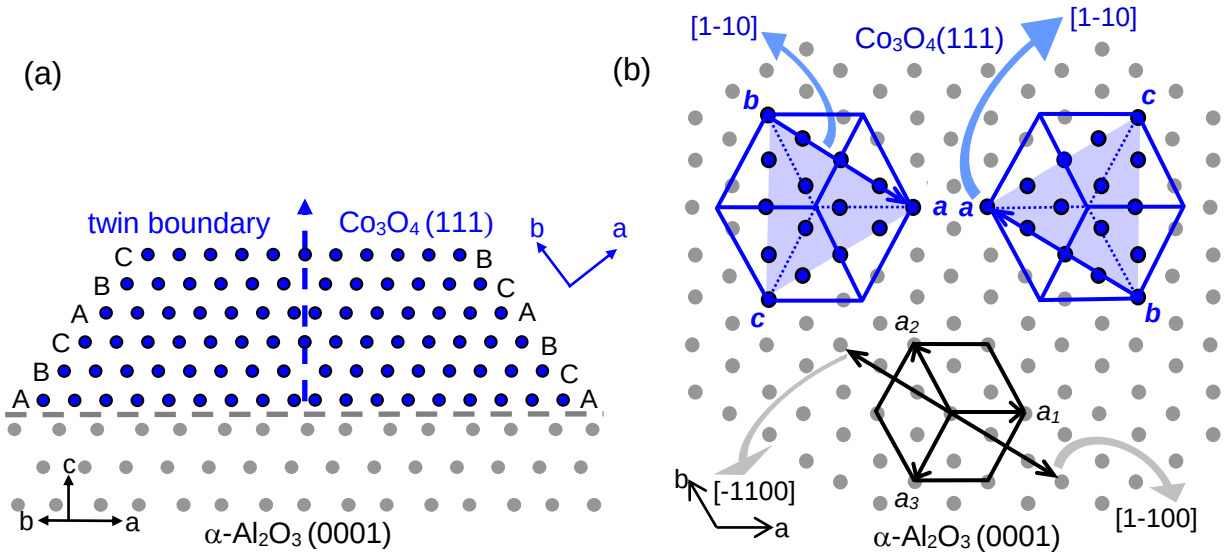

Figure 31. Schematic representation of two possible twin orientation diagram for (111) oriented spinel film: (a) the cross section view and (b) the top view.

The microstructure of thin film was analyzed by AFM and SEM techniques. Figure 32 presents cross-section view on NCO film (a) and after transformation on the Co_3O_4 spinel film (b). Figure 33 shows the surface morphology of Na_xCoO_2 and Co_3O_4 spinel film observed by AFM. Na_xCoO_2 film is formed by plate-like crystallite with longitudinal size of approximately 500-700 nm and the film thickness of around 600 nm. The crystallite shape changed during phase transformation as one can observe on images. Spinel film is build-up by columnar crystallites, which height (500 nm) also determines the film thickness. The thin film thickness contraction can be explained by the known fact that the annealing at higher temperatures leads generally to more dense material.

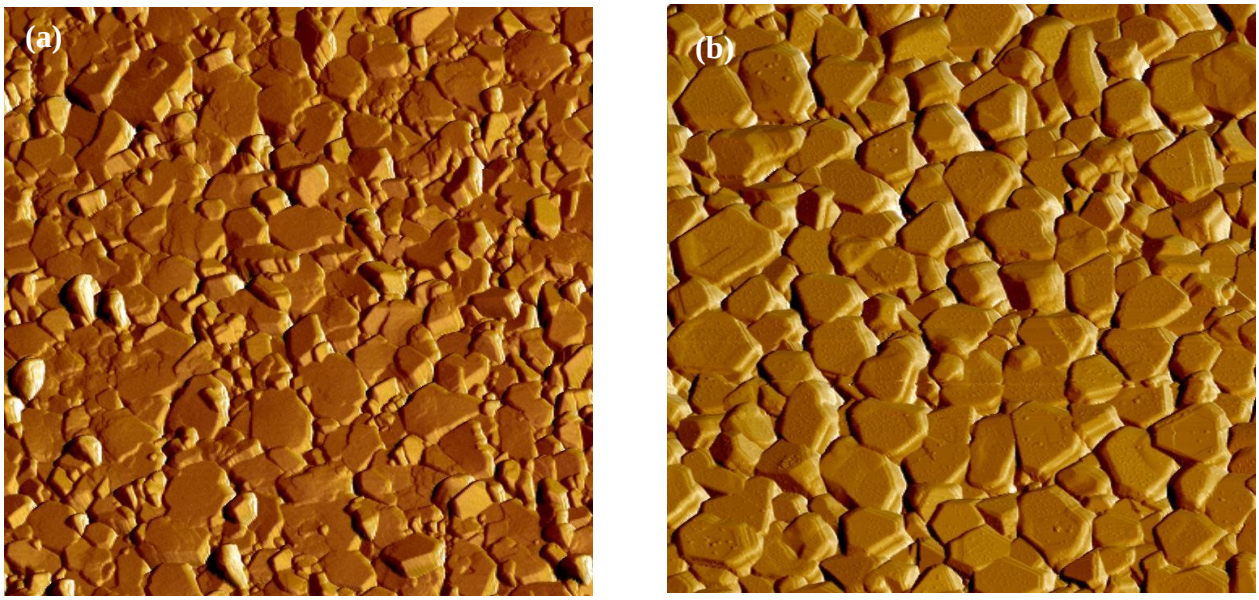

Figure 32. AFM morphology images from area 8 x 8μm: (a) Na_xCoO_2 (00l) thin film deposited on α-Al_2O_3 (00l) annealed at the temperature of 750 °C and (b) Co_3O_4 (111) thin film on α-Al_2O_3 (00l) obtained by heat treatment of Na_xCoO_2 (00l) thin film at 900 °C.

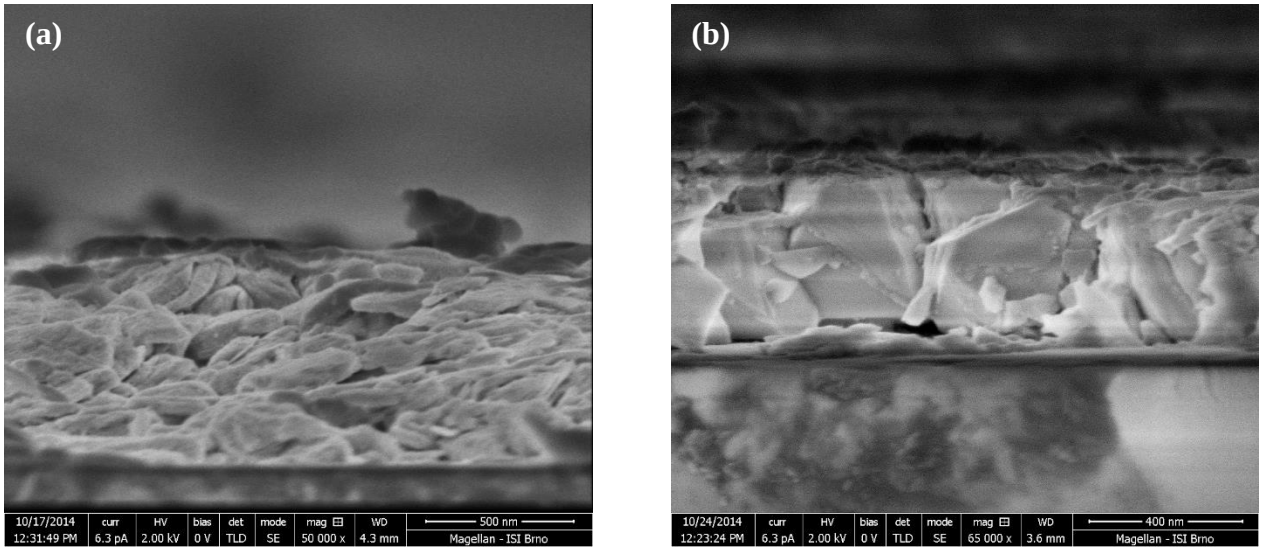

Figure 33. The cross section SEM images: (a) Na_xCoO_2 (00l) thin film deposited on α-Al_2O_3 (00l) annealed at the temperature of 750 °C and (b) Co_3O_4 (111) thin film on α-Al_2O_3 (00l) obtained by heat treatment of Na_xCoO_2 (00l) thin film at 900 °C.

The results gained on thin films can be summarized into following conclusions. Firstly, it was found that the stability of sodium cobaltate strongly depends on initial sodium stoichiometry and annealing temperature. We fund that the preparation of sodium cobaltate Na_xCoO_2 thin film

without impurities (Co_3O_4) is a difficult challenge, especially in the case of coating solutions with the low initial Na content (x = 0.175, and 0.35). We found that Na_xCoO_2 phase exhibits 00l oriented growth on α-Al_2O_3 irrespective of initial sodium content. The pure Na_xCoO_2 films were reached by using of the coating solutions with sodium stoichiometry x = 1.0 or 0.52 after annealing at the temperature of 750 °C and 800 °C. The higher annealing temperatures (850 and 900 °C) or the coating solutions with lower sodium stoichiometry (x = 0.35 and 0.175) leads to the formation of mixture of Na_xCoO_2 + Co_3O_4 phases or Co_3O_4 pure phase. We suggest that the formation of spinel is due to sodium volatility during the annealing. Similar effect we also observed for ceramic bulk samples. Moreover, in the case of the thin films, the diffusion of Na into the substrate can also play an important role in the formation of Co_3O_4, because in this case Na_xCoO_2 thin film is in direct contact with substrate.

The presence of Co_3O_4 depends on the annealing temperature and on the initial sodium stoichiometry x. The diffraction pattern of Co_3O_4 thin film prepared by deposition of the coating solution without Na also corresponds to the randomly oriented spinel. It was found that in the case of the series of Co_3O_4 thin films prepared from the coating solution with initial Na stoichiometry x = 0.175 (which is below the region of sodium cobaltate stability $x \geq 0.30$) the film is formed by randomly oriented Co_3O_4 phase. We found that the necessary condition for the oriented growth of Co_3O_4 is preliminary crystallization of Na_xCoO_2 followed by its decomposition. Spinel phase exhibited strong preferential orientation with the crystallographic planes *hhh* parallel to the substrate surface.

The condition for the preparation of pseudo-epitaxial Co_3O_4 film on α-Al_2O_3 was found. For Co_3O_4 thin films prepared from coating solution with initial sodium stoichiometry x = 0.5, the formation of twinning having the same out of plane orientation [111] with ⟨011⟩ and ⟨110⟩ planes rotated by 180° was observed. The higher FWHM values of maxima in the φ scans for Co_3O_4 films may be due to the fact, that the microstructure of CSD derived thin film is formed by high-temperature annealing procedure which cause the sintering and mass transport in the structure. The identical twin-growth on α-Al_2O_3 (00l) was observed also for other material with spinel structure like Fe_3O_4 prepared by CSD process [79].

The effect of self-assembly growth phenomena was also observed for another layered cobaltates $Bi_2Sr_2Co_2O_y$ [80] and for other plate-like shaped material from hexagonal crystal structure family e.g. ZnO [81] [82]. The oriented growth of layered cobaltate Na_xCoO_2 and

decomposition into the spinel structure as a novel preparation procedure was also studied on other substrates like MgO (100) and (111), $SrTiO_3$ (111), $LaAlO_3$ (111), and yttrium stabilized ZrO_2 (111) [paper 3] and we found that quite satisfactory results give MgO substrate. Using this substrate we succeeded to prepare both phases (Na_xCoO_2 and Co_3O_4) with in-plane orientation and we showed that the lattice mismatch between substrate and layer have the influence on the in-plane orientation.

7. Conclusion

The ceramic samples of Na_xCoO_2 were successfully prepared by Pechini method. The sodium stoichiometry in starting Na_xCoO_2 powders was in the range from $x = 0.7$ to 1.0. The phase composition was studied by PXRD for the samples heat-treated in the temperature range from 550 °C to 750 °C. The crystallization of rhombohedral α-Na_xCoO_2 phase started during calcination at 550 °C and pure α phase was obtained by the annealing at the temperature of 600 °C. The hexagonal γ-Na_xCoO_2 phase started to crystalize at the higher temperature of 650 °C and pure γ-Na_xCoO_2 phase without the rhombohedral phase can be obtained by the annealing at 750 °C. At the temperature of 750 °C, the minority phases Na_2CO_3 or Co_3O_4 was observed and their amount depend on initial sodium stoichiometry.

We found that in the final product, the sodium stoichiometry x of hexagonal phase Na_xCoO_2 is independent on sodium precursor amount in starting mixture and the samples heat treated at 750 °C crystalized preferably with sodium stoichiometry around $x = 0.65$ (determined from lattice parameter c). The elements quantity was determined by AAS and it showed that after final annealing at 750°C, the content of sodium in final products is lower in comparison with one in the nominal composition of precursor. The sodium losses are in the range from 15 mol% for the NCO _0.7/750 to 21 mol % for the NCO_1.0/750. We suggest that these loses are due to evaporation and/or reaction of sodium (in form of carbonates) with annealing crucible during pyrolysis and annealing procedure The long pyrolysis duration is necessary in order to remove the organic residues, which is not necessary for the standard solid state reaction between Co_3O_4 and sodium precursor where the rapid annealing method can be used.

Concerning the thermoelectric properties, it was found that the Seebeck coefficient depends on sodium content in Na_xCoO_2. The Seebeck coefficient at low temperatures (3 – 300 K) was experimentally determined and compared with calculated values for both series of the samples (α- and γ-phase). We found that for the series of samples annealed at 600 °C (containing only α-phase), the Seebeck coefficient correspond to value theoretically calculated for $x = 0.6$. In the case of γ-phase the experimentally determined values correspond to value theoretically calculated for $x = 0.7$. This can be explained by the fact that at higher temperature, more sodium atoms enter cobaltate structure. Two types of Seebeck coefficient behaviors bellow 50 K was observed and it indicates the presence of both positive and negative carriers, because the thermopower S is sensitive to the change in topology of a Fermi surface. From the comparison with published results, we can

conclude that sodium stoichiometry determined from Seebeck coefficient measurement of γ- phase is between 0.65 and 0.75.

Sodium cobaltate Na_xCoO_2 thin films on α-Al_2O_3 (00l) substrate were prepared by CSD method and the stability of Na_xCoO_2 on initial sodium stoichiometry *x* and on annealing temperature was studied by PXRD measurements. Sodium cobaltate films exhibited preferred orientation in the direction 00l that is in good agreement with films previously prepared by other authors. Decomposition of sodium cobaltate thin film into Co_3O_4 spinel structure was observed. The degree of decomposition depends on initial sodium stoichiometry *x* and on annealing temperature. Resulting Co_3O_4 exhibits preferential orientation with crystallographic planes *hhh* parallel to substrate. We found that under optimized conditions (initial sodium stoichiometry $x = 0.52$ and the annealing temperature of 900 °C) the pseudo-epitaxial Co_3O_4 thin film on α-Al_2O_3 (00l) substrate can be prepared by CSD method.

Oral presentation

1. M. Soroka, J. Buršik, R. Kužel: Oriented growth of Co_3O_4 (111) on α-Al_2O_3 by chemical solution deposition. *10th Interregional Workshop on Advanced Nanomaterials* (IWAN), Wroclaw, Poland. 2014.
2. M. Soroka, J. Buršik, R. Kužel, Preparation of Co_3O_4 films by thermal decomposition of Na_xCoO_2. *Structure 2015 with 11th student symposium*, Luhačovice, Czech Republic, 2015.

Papers

1. J. Buršík, M. Soroka, R. Kužel, F. Mika, Growth and characterization of thin oriented Co_3O_4 (111) films obtained by decomposition of layered cobaltates Na_xCoO_2, J. Solid State Chem. 227, 17 (2015).
2. J. Buršík, M. Soroka, K. Knížek, J. Hirschner, P. Levinský, J. Hejtmánek, Oriented thin films of $Na_{0.6}CoO_2$ and $Ca_3Co_4O_9$ deposited by spin-coating method on polycrystalline substrate, Thin Solid Films 603, 400 (2016).
3. J. Buršík, M. Soroka, R. Uhrecký, R. Kužel, F. Mika, Š. Huber, Thin (111) oriented $CoFe_2O_4$ and Co_3O_4 films prepared by decomposition of layered cobaltates, Appl. Surf. Sci. 376, 209 (2016).

References

[1] H Kawamotoa, SCIENCE & TECHNOLOGY TRENDS, 30 (2009) 54.

[2] J. R Sootsman, D. Y. Chung, M. G. Kanatzidis, Angewandte, 48 (2009) 8616.

[3] G. J.Snyder, E. S. Toberer, Nature 7 (2008) 105.

[4] J. Yang, T, Caillat, MRS BULLETIN 31 (2006) 224.

[5] T. M. Tritt, M. A. Subramanian, MRS BULLETIN 31 (2006) 188.

[6] S. B. Riffat, X. Ma, Applied Thermal Engineering 23 (2003) 913.

[7] C. Goupil, W. Seifert, K. Zabrocki, E. Müller, G. J. Snyder, Entropy 13 (2011) 1481.

[8] J. Zheng, Frontiers of Physics in China, 3 (2008) 269.

[9] I. Terasaki, Introduction to Thermoelectricity. (1998) 1–12.

[10] C. Wood, Reports on Progress in Physics 51 (1988) 459.

[11] A. B. C. Sales, D. Mandrus, R. K. Williams, Science, 272 (1996) 1325.

[12] M. Christensen, A. B. Abrahamsen, N. B. Christensen, F. Juranyi, N. H. Andersen, K. Lefmann, J. Andreasson, Ch. R. H. Bahl, B. B. Iversen, Nature materials, 7 (2008) 811.

[13] C. Uher, J. Yang, S. Hu, D. T. Morelli, G. P. Meisner, Physical Review B, 59 (1999) 8615.

[14] K. F. Hsu, S. Loo, F. Guo, W. Chen, J. S. Dyck, C. Uher, T. Hogan, E. K. Polychroniadis, M. G. Kanatzidis, Science, 303 (2004) 816.

[15] Y. F. Hu, E. Sutter, W. D. Si, Q. Li, Applied Physics Letters, 87 (2005) 171912.

[16] J. Hejtmánek, M. Veverka, K. Knížek, H. Fujishiro, S. Hebert, Y. Klein, A. Maignan, C. Bellouard, B. Lenoir, Materials Research Society Symposium Proceeding, 886 (2006) 35

[17] Y. Y. Wang, N. S. Rogado, R. J. Cava, and N. P. Ong ,Nature, 423 (2003) 425.

[18] M. R Apparao, J. Xiaohua, T. M. Tritt, MRS BULLETIN 3 (2006) 218.

[19] I. Terasaki, Y. Sasago, and K. Uchinokura, Physical Review B, 56 (1997) 12685.

[20] H. Yakabe, K. Kikuchi, I. Terasaki, Y. Sasago, and K. Uchinokura, Proceedings of the 16th International Conference on Thermoelectrics, (1997) 523.

[21] A W. Shin, N. Murayama, Journal of Materials Research, 15 (2011) 382.

[22] Y. Miyazaki, K. Kudo, M. Akoshima, Y. Ono, Y. Koike, and T. Kajitani, Japanese Journal of Applied Physics, 39 (2000) 531.

[23] T. Tsubota, M. Ohtaki, K. Eguchi, and H. Arai, Journal of Materials Chemistry, 7 (1997) 85.

[24] M. Ohtaki, K. Araki, K. Yamamoto, Journal of Electronic Materials, 38 (2009) 1234.

[25] C. Fouassier, G. Matejka, J.-M. Reau, P. Hagenmuller, Journal of Solid State Chemistry 6 (1973) 532.

[26] C. Delmas, C. Fouassier, P. Hagenmuller, Physica B+C, 99 (1980) 81.

[27] Y. Krockenberger, I. Fritsch, G. Christiani, H. U. Y. L. Habermeier, C. Bernhard, B. Keimer, L. Alff, Applied Physics Letters, 88 (2006) 162501.

[28] R. Berthelot, D. Carlier, C. Delmas, Nature Materials, 10 (2011) 74.

[29] M. L. Foo, Y. Wang, S. Watauchi, H. W. Zandbergen, T. He, R. J. Cava, and N. P. Ong, Physical Review Letters 92 (2004) 247001.

[30] M. Yokoi T. Moyoshi, Y. Kobayashi, M. Soda, Y. Yasui, M. Sato, K. Kakurai., Journal of Physical Society Japan, 74, (2005) 3046.

[31] Y. Maeno, H. Hashimoto, K. Yoshida, S. Nishizaki, T. Fujita, J. G. Bednorz, and F. Lichtenberg, Nature 372 (1994) 532.

[32] T. Motohashi, E. Naujalis, R. Ueda, K. Isawa, M. Karppinen, and H. Yamauchi, Applied Physics Letters, 79 (2001) 1480.

[33] T. Kawata, Y. Iguchi, T. Ito, K. Takahata, and I. Terasaki, Physical Review B, 60 (1999) 10584.

[34] T. Motohashi, R. Ueda, E. Naujalis, T. Tojo, I. Terasaki, T. Atake, M. Karppinen, H. Yamauchi. Physical Review B, 67 (2003) 064406.

[35] M. H. Whangbo, D. Dai, Inorganic Chemistry 45 (2006) 5989.

[36] F. C. Chou, J. H. Cho, Y. S. Lee, Physical Review B,70 (2004) 144526.

[37] B. C. Sales, R. Ji, K. A. Affholter, P. Khalifah, G. M. Veith, D. Mandrus, Physical Review B, 70 (2004) 174419.

[38] M. L. Foo, R. E. Schaak, V. L. Miller, T. Klimczuk, N. S. Rogado, Y. Wang, C. Craley, H. W. Zandbergen, N. P. Ong, R. J. Cava, Solid State Communications, 127 (2003) 33.

[39] Y. Lei, Xin Li, Lei Liu, G. Ceder, Chemistry of Materials, 26 (2014) 5288.

[40] L. Zhang, X. Tang, W Gao, Journal of Electronic Materials, 39 (2010) 1429.

[41] Q. Huang, M. L. Foo, R. A. Pascal, Jr.,J. W. Lynn, B. H. Toby, Tao He, H. W. Zandberger, R. J. Cava, Physical review B, 70 (2004) 184110.

[42] L. Viciu, J. W. G. Bos, H. W. Zandbergen, Q. Huang, M. L. Foo, S. Ishiwata, A. P. Ramirez, M. Lee, N. P: Ong, R. J. Cava, Physical review B, 73 (2006) 174104.

[43] H. Sakurai, S. Takenouchi, N. Tsujii, E. Takayama-Muromachi, Journal of the Physical Society, 73 (2004) 2081.

[44] C. Delmas, J.-J. Braconnier, C. Fouassier, P. Hagenmuller, Solid State Ionic, 3 (1981) 165.

[45] S. Kikkawa, S. Miyazaki, M. Koizumi, Journal of Solid State Chemistry, 62 (1986) 35.

[46] J. Y. Son, B. G. Kim, J. H. Cho, Applied Physics Letters, 86 (2005) 221918.

[47] J. Y. Son, H.-B.-R. Lee, J. H. Cho, Applied Surface Science, 254 (2007) 436.

[48] L. Yu, Y. Krockenberger, I. Fritsch, H. U. Habermeier, Progress in Solid State Chemistry, 35 (2007) 545.

[49] J. Y. Son, J. H. Cho, Journal of Crystal Growth, 310 (2008) 3093.

[50] L. Yu, L. Gu, Y. Wang, P. X. Zhang, H.-U. Habermeier, Journal of Crystal Growth, 328 (2011) 34.

[51] H. Ohta, S.-W. Kim, S. Ohta, K. Koumoto, M. Hirano, H. Hosono, Crystal Growth & Design, 5 (2005) 25.

[52] C.-J. Liu, P. K. Nayak, Y.-Z. Chen, Thin Solid Films 518 (2009) 91.

[53] H. Zhou, X. P. Zhang, B. T. Xie, Y. S. Xiao, C. X. Yang, Y. J. He, and Y. G. Zhao, Thin Solid Films, 497 (2006) 338.

[54] W. J. Chang, C. C. Hsieh, T. Y. Chung, S. Y. Hsu, K. H. Wu, T. M. Uen, J. Y. Lin, J. J. Lin, C. H. Hsu, Y. K. Kuo, H. L. Liu, M. H. Hsu, Y. S. Gou, J. Y. Juang, Appl. Applied Physics Letters, 90 (2007) 061917.

[55] A. E. Danks, S. R. Hall, Z. Schnepp, Material horizons, 3 (2016) 91.

[56] S. Sakka, Handbook of sol-gel science and technology. 1. Sol-gel processing, CHAPTER 4: Chemistry and Applications of Polymeric Gel Precursors (2005).

[57] Lone-Wen Tai, Journal of material research, 7 (1992) 502.

[58] Lone-Wen Tai, Journal of material research, 7 (1992) 511.

[59] J. C. R. Vossen. W. Kern, THIN FILM PROCESSES II, Elsevier (1991) Chapter: Sol-gel coating

[60] R. W. Schwartz, T. Schneller, R. Waser, R. C. Chimie 7 (2004) 433.

[61] F. F. Lange, Science, 273 (1996) 903.

[62] J. Rodriguez-Carvajal, Physica B, 192 (1993) 55.

[63] P. Blaha, K. Schwarz, G. K. H. Madsen, D. Kvasnicka, and J. Luitz, (Technische Universitat, Wien, 2001).

[64] G. K. H. Madsen and D. J. Singh, Computer Physic Communications 67 (2006) 175.

[65] T. Motohashi, R. Ueda, E. Naujalis, T. Tojo, I. Terasaki, T. Atake, M. Karppinen, H. Yamauchi, Physical Review B, 67 (2003) 064406.

[66] C. Ehrhardt, M. Gjikaj, W. Brockner, Thermochimica Acta, 432 (2005) 36.

[67] J. Plewa, K. Kozlowska, M. Sopicka-Lizer, A. Mrotzeka, E. Miillera, L Brunets, H. Altenburgr, 8th Workshop Thermoelectric, Cracow 2004.

[68] T. Motohashi, M. Karppinen, and H. Yamauchi Research Signpost, India, (2002) 73.

[69] Y. Okamota, A. Nishio, Z. Hiroi, Physical review B, 81 (2010) 121102.

[70] K. Knížek, J. Hejtmánek, M. Maryško, Z. Jirák, J. Buršík, K. Kirakci, P. Beran, Journal of Solid State Chemistry, 184 (2011) 2231.

[71] D. P. Chen, X. Wanga, Journal of Applied Physics, 103 (2008) 07C702.

[72] G. Lang, J. Bobroff, H. Alloul, P. Mendels, N. Blanchard, G. Collin, Physical Review B, 72 (2005) 094404.

[73] M.-H. Whangbo, D. Dai, Inorganic Chemistry, 45 (2006) 5989.

[74] K.G.Wilson, Rev.Mod.Phys. 47, (1975) 773.

[75] D. Yoshizumi, Y. Muraoka, Y. Okamoto, Y. Kiuchi, J.-I. Yamaura, M. Mochizuki, M. Ogata, Z. Hiroi, Journal of the Physical Society of Japan, 76 (2007) 063705.

[76] M. Gao, S. Zhou and Z Wang, Phys. Rev. 76, (2007) 180402.

[77] M. Burriel, G. Garcia, J. Santiso, A. Abruits, Z. Saltyte, A. Figueras, Chemical Vapor Deposition, 11 (2005) 106.

[78] M. Lie, K. Barnholt Klepper, O. Nilsen, H. Fjellvåg, A. Kjekshus, Dalton Trans. 2 (2008) 253.

[79] I. Yamaguchi, T. Terayama, T. Manabe, T. Tsuchiya, M. Sohma, T. Kumagai, S. Mizuta, Journal of Solid State Chemistry, 163 (2002) 239.

[80] X. Zhu, D. Shi, S. Dou, Y. Sun, Q. Li, L. Wang, Acta Material, 58 (2010) 4281.

[81] S.H. Yoon, D. J. Kim, Journal of Crystal Growth 303 (2007) 568.

[82] C.-Y. Zhang, X.-M. Li, X. Zhang, W.-D. Yu, J.-L. Zhao, Journal of Crystal Growth, 290 (2006) 67.